Thesis

Production cross sections of medical radioisotopes ^{52g}Mn and ^{198g}Au via charged-particle-induced reactions

(荷電粒子入射反応による医療用放射性同位体 ^{52g}Mn 及び ^{198g}Au の生成反応断面積)

6/30/2023

Hokkaido University

Damdinsuren Gantumur

Thesis

Production cross sections of medical radioisotopes ^{52g}Mn and ^{198g}Au via charged-particle-induced reactions

(荷電粒子入射反応による医療用放射性同位体 ^{52g}Mn 及び ^{198g}Au の生成反応断面積)

6/30/2023

Hokkaido University

Damdinsuren Gantumur

TABLE OF CONTENTS

Presented Paper List and Conference Presentation List

Part of this study was presented in the following papers:

1. Damdinsuren Gantumur, Masayuki Aikawa, Tegshjargal Khishigjargal, Erdene Norov, Shuichiro Ebata, Hiromitsu Haba "Production cross sections of ^{52}Mn in alpha-particle-induced reactions on natural vanadium" Applied Radiation and Isotopes, 184 (2022), 110204. https://doi.org/10.1016/j.apradiso.2022.110204
2. Damdinsuren Gantumur, Masayuki Aikawa, Tegshjargal Khishigjargal, Erdene Norov, Naoyuki Ukon, Hiromitsu Haba "Activation cross sections of proton-induced reactions on natural platinum up to 30 MeV" Applied Radiation and Isotopes, 192 (2023), 110621. https://doi.org/10.1016/j.apradiso.2022.110621

Part of this study was presented at the following academic conferences:

1. G. Damdinsuren, M. Aikawa, Kh. Tegshjargal, N. Erdene, S. Ebata, H. Haba "Production cross sections of ^{52}Mn in alpha-particle-induced reactions on natural vanadium" RIKEN Accelerator Progress Report 55 (2022) 156.
2. Gantumur DAMDINSUREN, Masayuki AIKAWA, Khishigjargal TEGSHJARGAL, Norov ERDENE, Naoyuki UKON, and Hiromitsu HABA "Production cross sections of ^{198g}Au in proton-induced reactions on natural platinum" 2022 Symposium on Nuclear Data, November 17-18 (2022), Kindai University, Osaka, Japan.
3. Gantumur Damdinsuren, Masayuki Aikawa, Khishigjargal Tegshjargal, Norov Erdene, Naoyuki Ukon, and Hiromitsu Haba "Production cross sections of ^{198g}Au in proton-induced reactions on ^{nat}Pt" AESJ Hokkaido Branch 40th Research Presentation Meeting on February 17 (2023), Hokkaido University, Sapporo, Japan.

List of Abbreviations

The abbreviations used in the body text and figures are as follows:

AVF	Azimuthally Varying Field
CT	Computed Tomography
EC	Electron Capture
HPGe	High Purity Germanium
IAEA	International Atomic Energy Agency
IT	Isomeric Transition
LET	Linear Energy Transfer
LINAC	Linear Accelerators
MRI	Magnetic Resonance Imaging
PET	Positron Emission Tomography
PHY	Physical Yield
RI	Radioactive Isotope
SPECT	Single-Photon Emission Computed Tomography
SRIM	Stopping and Range of Ions in Matter
TAT	Targeted Alpha Therapy
TENDL	TALYS-based Evaluated Nuclear Data Library
TOF	Time-Of-Flight

CHAPTER 1: INTRODUCTION

1.1 Nuclear medicine

George de Hevesi was a Hungarian physician who first used radioactive isotopes in bone studies in 1924. This is considered the beginning of nuclear medicine, which uses small amounts of radioactive material to diagnose and treat diseases (Myers, 1979). In 1932, Ernest O. Lawrence, an American physicist, invented the first cyclotron. The invention of the cyclotron was a breakthrough in nuclear physics and paved the way for developing other types of particle accelerators. It also played an important role in developing nuclear medicine by producing radioisotopes for medical use (Lawrence & Livingston, 1932). The first medical cyclotron was installed in 1951 at the University of California, Berkeley. The cyclotron produced isotopes for medical use, such as phosphorus-32 and sulfur-35. These isotopes were used for research purposes, and the production of isotopes for diagnostic and therapeutic purposes did not become more common in the following years.

After World War II, many countries shifted their focus from military uses of nuclear energy to peaceful applications. One of these applications was the production of isotopes for medical use. Nuclear reactors can be used to produce isotopes through neutron activation. This made the use of isotopes in medicine more widespread and contributed to the development of new nuclear medicine techniques (International Atomic Energy Agency, 2003).

Modern nuclear medicine is a rapidly growing medical sector that uses small amounts of radioactive nuclides, called radioactive materials, to diagnose and treat diseases. Nuclear medicine imaging procedures use small amounts of radioactive materials, called tracers, which are introduced into the body by injection, inhalation, or ingestion. These tracers travel through the body and give off energy in the form of emitted gamma rays, which are detected by a special camera to create images of the inside of the body. Nuclear medicine imaging can show the function and structure of organs and systems inside the body and help diagnose and treat many diseases.

1.2 Applications of medical radioisotopes

Radioisotopes and radioactive materials are widely used in the medical field for various purposes. They are used in diagnostic procedures, such as imaging scans (e.g., PET and SPECT scans), to help to detect and diagnose diseases. They are also used in therapy to treat certain types of cancer, such as thyroid and prostate cancer, by delivering a targeted dose of radiation to the affected area. Additionally, the concept of theranostics, which combines diagnostic and therapeutic applications, is becoming more popular in the medical field. This uses radioisotopes to diagnose and treat disease simultaneously, improving patient outcomes and reducing the overall cost of care.

1.2.1 Diagnostic applications

Positron emission tomography (PET) and single-photon emission computed tomography (SPECT) are two of the most used nuclear imaging techniques in nuclear medicine. They both use radioisotopes to produce detailed images of the internal structures and functions of the body (van Dort et al., 2008). One of the main advantages of nuclear medicine diagnosis is its ability to detect lesions and abnormalities earlier than other imaging methods. Nuclear medicine imaging can detect changes in the body's cellular and metabolic activity, indicating the presence of disease long before other imaging methods such as X-ray or Computed Tomography (CT) can see structural changes. Another significant feature of nuclear medicine is its ability to specifically show the locations and sizes of tumors, especially when combined with CT or Magnetic Resonance Imaging (MRI).

The radioisotopes of short half-lives and low-energy positron emitters are suitable for PET applications. Short-lived positron emitters (^{11}C, ^{13}N, ^{15}O, and ^{18}F) are mainly used at production sites and nearby hospitals. Two widely used positron emitters produced via generator systems in nuclear medicine are ^{68}Ga and ^{82}Rb. Their parent nuclides ^{68}Ge ($T_{1/2}$ = 271 d) and ^{82}Sr ($T_{1/2}$ = 25.3 d) are long-lived. There are several commonly used radioisotopes in PET imaging, and their data, such as their half-life, decay mode, and production methods, are summarized in Table 1.1.

Fluorine-18 is a commonly used radioisotope in PET scans. Its half-life of 109.8 min is compatible with a typical imaging period, resulting in safe radiation exposure for patients. (Alauddin, 2012). The production of ^{18}F on a low-energy cyclotron makes it an accessible and cost-effective option for many medical facilities. ^{18}F production can be done by two main routes: ^{18}O(p,n)^{18}F and ^{nat}Ne(d,x)^{18}F reactions. The ^{18}O(p,n)^{18}F reaction is the most common method of ^{18}F production, which is done by bombarding a target of ^{18}O with protons from a medical cyclotron.

Table 1.1. The commonly used radionuclides (positron emitters) for Positron Emission Tomography (PET) imaging

Radionuclide	Half-life	Decay mode (%)	<E(β^+)> (keV)	I(β^+) (%)	Production method
^{11}C	20.364 min	β^+ (100)	385.7	99.7669	Cyclotron
^{13}N	9.965 min	β^+ (100)	491.82	99.8036	Cyclotron
^{15}O	122.24 s	β^+ (100)	735.28	99.9003	Cyclotron
^{18}F	109.77 min	β^+ (100)	249.8	96.73	Cyclotron
^{68}Ga	67.71 min	$\varepsilon + \beta^+$ (100)	829.5	88.91	^{68}Ge/^{68}Ga generator
^{82}Rb	1.2575 min	$\varepsilon + \beta^+$ (100)	1481	95.4	^{82}Sr/^{82}Rb generator

Single photon emission computed tomography (SPECT) is a nuclear medicine imaging modality that uses gamma rays emitted from radiotracers to create detailed images of the inside of the body. The radionuclides emit gamma rays in the energy of 100-200 keV through either the process of electron capture (EC) or isomeric transition (IT) are used. This energy range is suitable for SPECT imaging. Commonly used radioisotopes in SPECT imaging, and their data, such as their half-life, decay mode, and production methods, are summarized in Table 1.2.

^{99m}Tc emits 140 keV gamma rays and is a widely used radionuclide in SPECT imaging (Boros et al., 2014). In a hospital, ^{99m}Tc is obtained via the ^{99}Mo/^{99m}Tc generator system. The parent nuclide ^{99}Mo ($T_{1/2}$ = 66.0 h) is mainly produced in a nuclear reactor. The reactor has two production routes as ^{98}Mo(n,γ)^{99}Mo and ^{235}U(n,f)^{99}Mo. Another possible route to produce ^{99}Mo is through an alpha-particle-induced reaction on zirconium (Zr) using a cyclotron (Murata et al., 2019). However, this method is still under development and has not yet been commercialized.

Table 1.2. Common radionuclides (gamma emitters) for SPECT applications

Radionuclide	Half-life	Decay mode (%)	E_γ (keV)	I_γ (%)	Production method
^{67}Ga	3.2617 d	ε (100)	93.31	38.81	Cyclotron
			184.58	21.41	
			300.22	16.64	
^{99m}Tc	6.0067 h	IT (100)	140.511	89	^{99}Mo/^{99m}Tc generator
^{111}In	2.8047 d	ε (100)	171.28	90.7	Cyclotron
			245.35	94.1	
^{123}I	13.2235 h	ε (100)	159.0	83.6	Cyclotron
^{201}Tl	3.0421 d	ε (100)	135.34	2.61	Cyclotron
			167.43	10.0	

1.2.2 Therapeutic applications

Therapeutic radioisotopes use radiation with high linear energy transfer (LET), such as Auger electrons, beta particles, and alpha particles. The tissue range of a particle depends on both the LET and the particle energy. Particles with high LET and a short tissue range are more effective for biological and chemical damage. Particles of a long tissue range can be used to treat large tumors (Kassis, 2008).

Alpha particles have high energy (5-8 MeV), high LET (~80 keV/μm), and a short range (40-100 μm) in tissue. Their highly ionizing capacity and short tissue range make alpha particles suitable for targeted alpha therapy (TAT). Beta particles emitted from some radionuclides can cover a wide-energy range (0.1-2.2 MeV), a relatively low LET (0.2 keV/μm), and a high tissue range (0.5-10 mm) (Kostelnik & Orvig, 2019; Ramogida & Orvig, 2013). Auger electrons have high LET values (4-26 keV/μm), low energy (1-10 keV), and a short tissue range (1-20 μm) (Buchegger et al., 2006). Commonly used therapeutic isotopes and their data are summarized in Table 1.3.

Table 1.3. Most common radioisotopes (alpha, beta, auger electron emitters) for therapeutic applications

Radionuclide	**Half-life**	**Decay (%)**	**E (keV)**	**Production method**
		Alpha emitters		
^{211}At	7.214 h	α (41.80)	5869.5	Cyclotron
^{212}Bi	60.55 min	α (35.94)	6050.78 6089.88	^{228}Th/^{212}Bi generator
^{213}Bi	45.61 min	α (2.20)	5558 5875	^{225}Ac/^{213}Bi generator
^{225}Ac	9.920 d	α (100)	5792.5 5830	^{233}U decay/cyclotron
		Beta emitters		
^{64}Cu	12.701 h	β^- (38.5)	<191>	Reactor & cyclotron
^{67}Cu	61.83 h	β^- (100)	<141 >	Reactor & cyclotron
^{90}Y	64.053 h	β^- (100)	<932.3>	^{90}Sr/^{90}Y generator
^{131}I	8.0252 d	β^- (100)	<181.9>	Reactor
^{177}Lu	6.647 d	β^- (100)	<133.6 >	Reactor & cyclotron
^{186}Re	3.7186 d	β^- (92.53)	<348.0 >	Reactor & cyclotron
		Auger electron emitters		
^{67}Ga	3.2617 d	AE (3.1)	<6.3>	Cyclotron
^{123}I	13.2235 h	AE (3.7)	<7.4>	Cyclotron
^{125}I	59.407 d	AE (19.9)	<12.2>	Cyclotron

1.2.3 Theranostic applications

The isotopes used simultaneously for diagnostic and therapeutic purposes are known as "theranostic radionuclides." They have both diagnostic and therapeutic capabilities, and they can be used at the same time. This approach is more efficient than traditional diagnose and treatment procedures. Several radionuclides are available for theranostic applications (Srivastava, 2012). Some well-established therapeutic radionuclides are also being explored for theranostic applications, such as ^{47}Sc, ^{90}Y, ^{131}I, ^{166}Ho, ^{177}Lu, ^{188}Re, and ^{213}Bi. These radionuclides have properties that allow for both imaging and therapy. However, more research and clinical trials are needed to establish their safety and efficacy for theranostic applications. Both ^{124}I and ^{64}Cu are commonly used in medical imaging and can also be used for radiation therapy.

Radionuclides for PET or SPECT can be combined with therapeutic isotopes to form theranostic pairs (Werner et al., 2015). Some potential radionuclides suitable for theranostic pairs are ^{44}Sc/^{47}Sc, ^{64}Cu/^{67}Cu, ^{68}Ga/^{67}Ga, ^{72}As/^{77}As, ^{83}Sr/^{89}Sr, ^{86}Y/^{90}Y, ^{110g}In/^{111}In, ^{124}I/^{131}I, ^{152}Tb/^{161}Tb, and ^{152}Tb/^{149}Tb (Baum & Kulkarni, 2012; Qaim et al., 2018).

1.3 Production of medical radioisotopes

The production of medical radionuclides is important for practical use. The main processes to produce medical radioisotopes and radioactive materials are neutron activation, nuclear fission, charged-particle-induced reactions, and radionuclide generators. Cyclotrons and nuclear reactors are commonly used for radionuclide production (International Atomic Energy Agency, 2003, 2009; Qaim, 2012). Linear accelerators (LINAC) also can be used for medical radionuclide production but are far less common (Starovoitova et al., 2014).

The production of isotopes through a nuclear reaction depends on the number of target atoms, the intensity of the particle beam, and the probability of the nuclear reaction. The number of target atoms and beam intensity are measurable and controllable parameters. The number of target atoms can be determined by measuring the weight and volume of the target material, while detectors or other instruments can measure the intensity of the particle beam. These values and cross sections of the reaction are used to calculate the expected production rates of isotopes. The cross sections of a nuclear reaction are the probability to induce the reaction and depend on the energy of the incident particles. The cross sections are typically obtained through experiments and are often provided as a function of energy. The cross sections and beam energy are important factors affecting the yield and radionuclidic purity of isotopes produced in a nuclear reaction.

1.3.1 Reactor production

Nuclear reactors are used to produce radioisotopes by neutron-induced reactions. The reactions occur with charged-particle emission, gamma emission, and fission prosses. The (n,γ) reaction, also known as neutron capture, is commonly used in the production of radionuclides. It has a higher cross section at thermal neutron energy compared to other neutron-induced reactions such as (n,p), (n,α), or (n,2n) reactions (Mausner et al., 1998). This process can produce a wide range of radionuclides, such as ^{99}Mo and ^{192}Ir. ^{99}Mo is the parent of ^{99m}Tc used in over 80% of all medical imaging procedures and ^{192}Ir is used in brachytherapy to treat cancer. One limitation of the (n,γ) reaction for isotope production is that it results in low specific activity. The specific activity of an isotope produced through the (n,γ) reaction is usually lower than those of isotopes produced through fission and charged-particle-induced reactions. This can be a limitation in some applications where small amounts and high specific activity of radioactive isotopes are needed. In some research and advanced reactors, higher energy neutrons can produce radioisotopes through other channels, such as (n,p) and (n,α) reactions. The disadvantage of these reactions is lower cross sections than those of the (n,γ) reactions. The reactions can only be used to produce some special radionuclides, especially elements

of the light mass region. (International Atomic Energy Agency, 2003; S.M. Qaim et al., 2012). In nuclear reactors, several widely used medical isotopes, such as ^{90}Sr, ^{99}Mo, ^{131}I, and ^{133}Xe, are produced using fission. One of the significant disadvantages of the fission process is that it generates large quantities of radioactive waste material.

1.3.2 Accelerator production

Nuclear reactions induced by charged particles (p, d, ^{3}He, α) accelerated at cyclotrons have some advantages. These reactions can produce isotopes that are not easily accessible through other methods, such as (n,γ) or fission reactions. They can also produce isotopes with high specific activity because the product can be a different element from the target, providing more opportunities for chemical and physical separation procedures (Qaim, 2004). Another significant advantage of charged-particle-induced reactions is the smaller amount of radioactive waste generated than other production methods, such as nuclear reactors. Research and applications in producing medical isotopes by charged-particle-induced reactions have increased rapidly in recent years. Medical radioisotopes for production by charged-particle-induced reactions on cyclotrons are summarized in Table 1.4.

Table 1.4. Medical radioisotopes for production on cyclotrons (Benešová & Reischl, 2022; Engle et al., 2019; IAEA - Medical portal)

Positron emitters (PET)	**Gamma emitters (SPECT)**	**Therapeutic radionuclides**
^{11}C, ^{13}N, ^{15}O, ^{18}F ^{44}Sc, ^{52m}Mn, ^{52g}Mn, ^{55}Co, ^{61}Cu, ^{62}Cu, ^{64}Cu ^{66}Ga, ^{68}Ga, ^{72}As, ^{73}Se, ^{76}Br, ^{82m}Rb, ^{82g}Rb, ^{86}Y, ^{89}Zr, ^{90}Nb, ^{94m}Tc, ^{110m}In, ^{118}Sb, ^{120}I, ^{122}I, ^{124}I, ^{128}Cs, and ^{140}Pr	^{51}Cr, ^{67}Ga, ^{81}Rb, ^{99m}Tc, ^{111}In, ^{123}I, ^{178}W, and ^{201}Tl	^{64}Cu, ^{67}Cu, ^{67}Ga, ^{86}Y, ^{103}Pd ^{111}In, ^{114m}In, ^{124}I, ^{125}I, ^{131}Cs, ^{169}Yb, ^{177}Lu, ^{186}Re, ^{192}Ir, ^{211}At, ^{225}Ac, ^{227}Th, and ^{230}U

1.3.3 Radionuclide generators

In generator systems, we can use short-lived daughter nuclides decayed from long-lived parent nuclides for medical applications. The parent and daughter nuclides in a generator system are different elements. This property makes chemical separation easier and provides pure isotopes. Parent nuclides for generator systems are produced using nuclear reactors or cyclotrons. Some generator systems are used for clinical applications, such as ^{99}Mo/^{99m}Tc, ^{82}Sr/^{82}Rb, ^{90}Sr/^{90}Y, ^{68}Ge/^{68}Ga, ^{72}Se/^{72}As, and ^{52}Fe/^{52m}Mn (Boros & Packard, 2019; Pijarowska-Kruszyna et al., 2022).

1.4 Purpose of the study

The production of radionuclides is essential for practical use. Cross sections are fundamental data for production. The cross sections of charged-particle-induced reactions are of great interest for many application fields, such as nuclear physics, nuclear medicine, and radiation protection. The measurement of the cross sections can help to understand the behavior of nuclear systems and predict the yield of specific isotopes.

This study aims to measure cross sections (excitation functions) for the production of medical radioisotopes via charged-particle-induced reactions. This study can help to understand the most efficient routes in a nuclear facility and to optimize the production process.

The experiments were performed at the AVF cyclotron of the RIKEN RI Beam Factory. We adopted well-established stacked-foil activation techniques and gamma-ray spectrometry to determine activation cross sections. The following two experiments were performed.

In the first experiment, the excitation functions of the alpha-particle-induced reactions on ^{nat}V were determined up to 50 MeV, with a particular focus on the ^{52g}Mn production. ^{52g}Mn is a radioisotope for PET imaging. It has a half-life of about 5.6 days and decays by emitting a positron. Using ^{52g}Mn in PET imaging allows studying biological and physiological processes with a time scale similar to its decay. The main goal of this experiment was to discuss the possible route of producing ^{52g}Mn from ^{nat}V and the optimal conditions for the production process.

In the second experiment, the excitation functions of the proton-induced reactions on ^{nat}Pt were determined up to 30 MeV, with a particular focus on the ^{198g}Au production. ^{198g}Au has a half-life of 2.6941 d and is a beta emitter (β^-: 100%, $<E_\beta->$ = 312.5 keV). ^{198g}Au is widely used for therapy in nuclear medicine, specifically cancer treatment. The experimental results can contribute to the production optimization of ^{198g}Au.

CHAPTER 2: EXPERIMENTAL METHODS

The experiments were performed at the AVF cyclotron of the RIKEN RI Beam Factory. The activation cross sections of charged-particle-induced reactions were measured using well-established methods of stacked-foil activation technique and high-resolution gamma-ray spectrometry.

Fig. 2.1. RIKEN Azimuthally Varying Field (AVF) Ring Cyclotron

2.1 Activation cross section measurement

A nuclear reaction is a process in which the nucleus of an atom interacts with another nucleus. This can occur through various mechanisms, including nuclear fusion and fission. Nuclear reactions can be represented by equations similar to those used for chemical reactions. If a target nucleus X is bombarded by a particle x and results in a nucleus Y with an emitted particle y, this is commonly written in one of two ways,

$$x + X \rightarrow Y + y \tag{2.1}$$

or

$$X(x, y)Y \tag{2.2}$$

The cross section (σ) is proportional to the probability that the nuclear reaction occurs. The cross section represents the effective area where the incoming particle interacts with the target and induces the reaction. The larger the cross section, the more the reaction probability. The cross section depends on many factors, such as the energy of the incoming particle, the target nucleus, and the type of reaction. The reaction cross section of the $X(x, y)Y$ reaction at the incident energy E_i is proportional to the ratio of the numbers of induced and produced particles.

$$\sigma(E_i) \propto \frac{N_y}{N_x} \tag{2.3}$$

Direct (online) detection and spectroscopic (offline) identification methods are two commonly used techniques for measuring nuclear reaction cross sections. The direct detection method measures the energy and angle of the emitted particle. The disadvantage of this method is the difficulty to distinguish the produced particles from different reactions. Another disadvantage is the inclusion of expensive techniques and devices.

The spectroscopic identification method identifies the radioactive isotopes produced by the reaction and determines the cross section from the measured activity. In this method, one of the most common techniques is gamma-ray spectrometry. Gamma-ray spectrometry is a technique that uses a detector to measure the energy and intensity of the gamma rays emitted by the decay of the radioactive nuclei. The gamma-ray spectrometer typically consists of a detector, such as a scintillation detector or a germanium detector, and a data acquisition system.

2.1.1 Calculation of the activation cross sections

The reaction rate Y (#/s) is a measure of the number of produced nuclei per second in a nuclear reaction. It can be derived from the reaction cross section, the incident beam intensity, and the target number density. The reaction rate can be written as:

$$Y = \sigma \cdot n_T \cdot I \tag{2.4}$$

$$n_T = \frac{\rho \cdot N_A}{A_T} \cdot L \tag{2.5}$$

where σ is a cross section (cm^2), I (#/s) and n_T (#/cm^2) are the beam intensity and the number of target particles per unit surface density of the target, ρ is the density of the target material (g/cm^3), N_A is Avogadro constant (#/mol), A_T is the molar mass of the target (g/mol), L is the target thickness (cm).

If the produced nuclide by a nuclear reaction is unstable, it decays during irradiation. In this case, the reaction rate can be described by considering the decay of the produced nuclide. The reaction rate can be written as follows:

$$\frac{dN(t)}{dt} = Y - \lambda \cdot N(t) \tag{2.6}$$

$$\lambda = \frac{\ln 2}{T_{1/2}} \tag{2.7}$$

where λ is the decay constant of a radionuclide (#/s), $T_{1/2}$ is the half-life of a radioactive nucleus (s).

The number of radioactive nuclei produced during the irradiation period (T_b) can be calculated as follows:

$$N(0) = Y \cdot \frac{(1 - e^{-\lambda T_b})}{\lambda} \tag{2.8}$$

The gamma lines from the decay of radioactive nuclides can be measured by an HPGe detector during the acquisition time (T_m) after the cooling time (T_c). The number of measured counts (ΔN) can be related to the number of radioactive nuclei produced during the irradiation period as follows:

$$\Delta N = \varepsilon_d \cdot \varepsilon_\gamma \cdot \varepsilon_t \cdot N(0) \cdot e^{-\lambda T_c} \cdot (1 - e^{-\lambda T_m}) \tag{2.9}$$

where ε_d is the detector efficiency, ε_γ is the gamma-line intensity, ε_t is the dead time correction.

$$\varepsilon_t = \frac{T_m - T_{dead\ time}}{T_m} = \frac{T_{live\ time}}{T_{real\ time}} \tag{2.10}$$

Finally, the production cross sections can be derived from Equations (2.4), (2.8), and (2.9) as follows.

$$Y = \frac{\Delta N \cdot \lambda}{\varepsilon_d \cdot \varepsilon_\gamma \cdot \varepsilon_t \cdot (1 - e^{-\lambda T_b}) \cdot e^{-\lambda T_c} \cdot (1 - e^{-\lambda T_m})} \tag{2.11}$$

$$\sigma = \frac{\Delta N \cdot \lambda}{n_T \cdot I \cdot \varepsilon_d \cdot \varepsilon_\gamma \cdot \varepsilon_t \cdot (1 - e^{-\lambda T_b}) \cdot e^{-\lambda T_c} \cdot (1 - e^{-\lambda T_m})} \tag{2.12}$$

2.2 Stacked foil activation technique

The stacked-foil activation technique is a method to measure the energy-dependent cross sections (excitation functions) of nuclear reactions induced by light ions (p, d, ^{3}He, α) (Sonzogni et al., 1992). The excitation function is a measure of the probability of a certain reaction as a function of the incident energy. To obtain accurate excitation functions, the incident energy and the flux of the beam must be determined accurately.

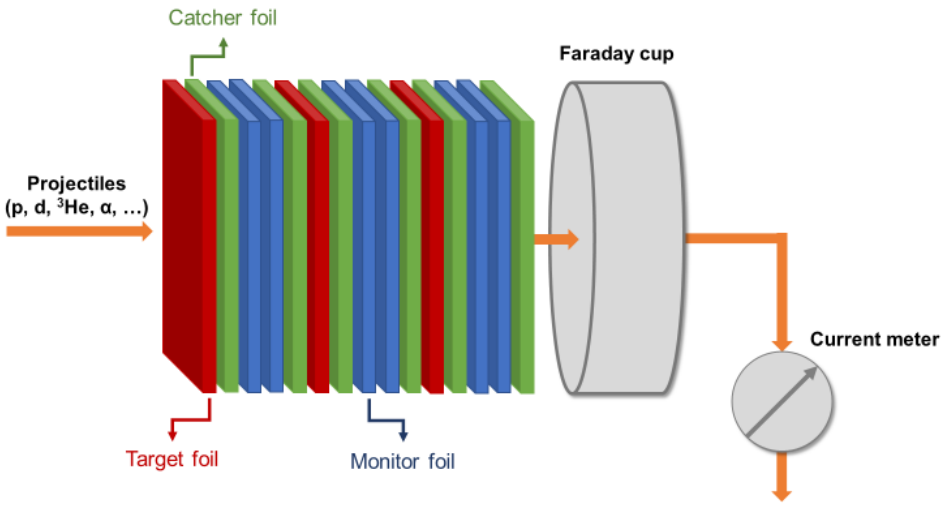

Fig. 2.2. The schematic diagram of the experimental setup of the stacked-foil activation technique

In this technique, the target is composed of several foils of different materials. The schematic diagram of the experimental setup of the stacked foil activation technique is shown in Fig. 2.2. The energy of the beam at each foil is different from the others. As the beam passes through the foils, its energy is partly absorbed by the material and decreased. To reduce the spread and loss of energy, thin foils are chosen. A stack of foils in the technique often consists of four types of foils: the main target, monitor, catcher, and energy-degrader foils.

The main target foil is selected for the reaction of interest. Monitor foils are used to assess beam parameters and target thicknesses. The monitor foils should differ from the target material. Energy-degrader foils gradually reduce the beam energy along the stack. Catcher foils are used to catch the reaction of recoiled products. The catcher should be low atomic number material to decrease gamma-ray attenuation during activity measurements (Sonzogni et al., 1992). Moreover, catcher and degrader foils should not produce the same radioisotopes as the target in the stack. Aluminum (Al) foil is commonly used for catcher and degrader foils.

In our experiments, the primary beam energy was measured by the time-of-flight method (Watanabe et al., 2014). The beam intensity was measured by the Faraday cup, as shown in Fig. 2.3.

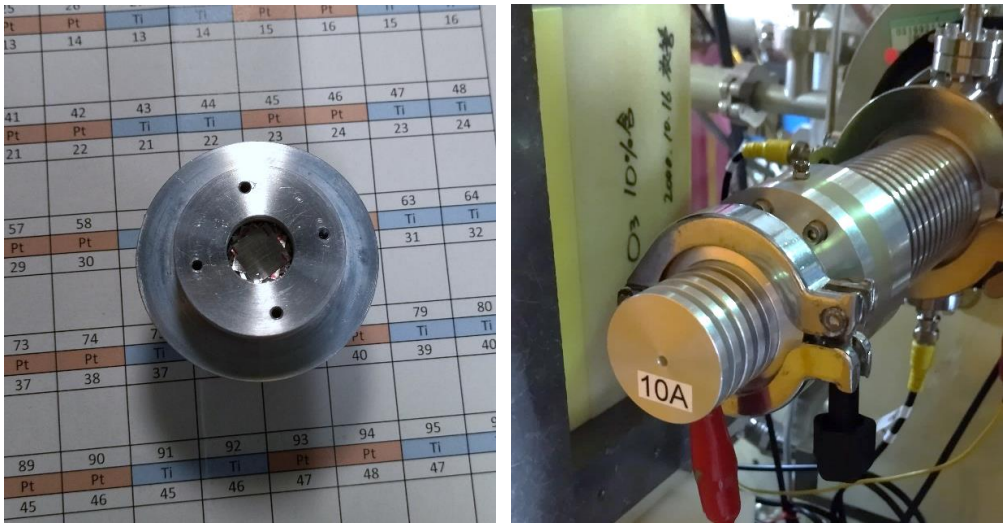

Fig. 2.3. (a) Faraday cup like target holder; and (b) Target holder set on beam line

2.2.1 Energy degradation calculation

The energy degradation in the stacked target was calculated using the SRIM code (Ziegler et al., 2010). SRIM, the Stopping and Range of Ions in Matter, is a collection of software packages that calculate many features of the transport of ions in matter. Most aspects of the energy loss of ions in the matter can be calculated. SRIM can quickly produce stopping powers, range, and straggling distributions if projectile, energy, and target are defined.

Charged particles passing through matter continuously interact with the electrons and nuclei of atoms and lose their energy. Stopping powers refer to an energy loss of charged particles in matter. Linear stopping power $S(E)$ (MeV/cm) describes the average energy loss of projectiles per unit length in the target.

$$S(E) = \frac{dE}{dx} \tag{2.13}$$

The mass-stopping power $S_m(E)$ (MeV/(mg/cm^2)) can be described by the linear stopping power divided by the material density ρ (g/cm^3).

$$S_m(E) = dE / d(\rho x) \tag{2.14}$$

The total stopping power is the sum of the electron $S_e(E)$ and nuclear-stopping powers $S_n(E)$:

$$S_{tot}(E) = S_e(E) + S_n(E) \tag{2.15}$$

For example, the mass-stopping power of alpha particles on vanadium using the SRIM code is shown in Fig. 2.4.

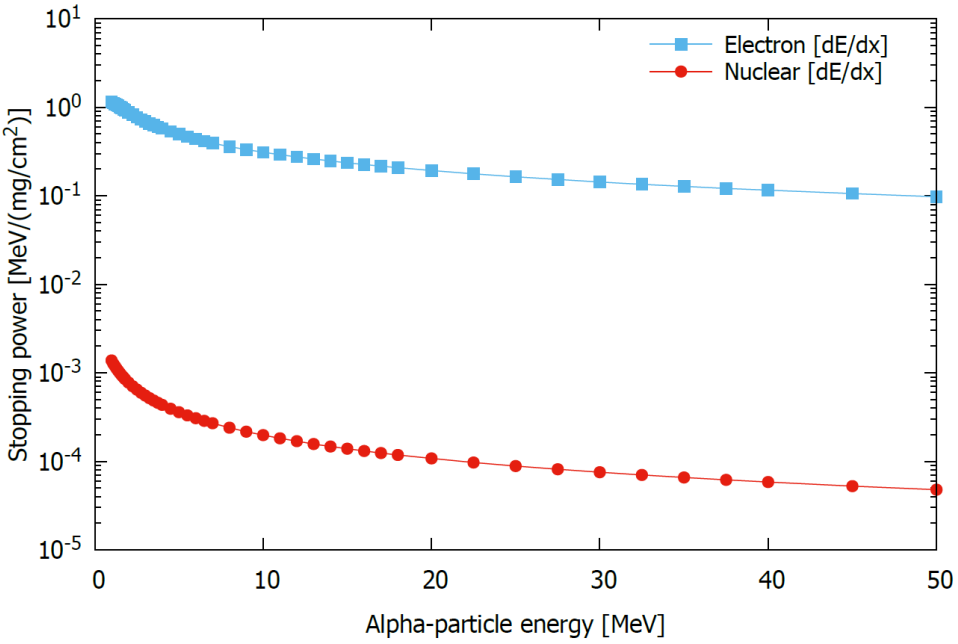

Fig. 2.4. The stopping powers of alpha particles on vanadium

We calculated the energy degradation using the stopping powers. The relation between the average thickness of foil and the stopping power can be expressed as follows:

$$\rho x = \int_{E_{in}}^{E_{out}} \frac{1}{S(E)} dE \tag{2.16}$$

where E_{in} and E_{out} are incident and outgoing energy, respectively.

The SRIM code produces the discrete values of stopping powers. The stopping power can be assumed as a linear function in a thin foil.

$$S(E) = aE + b \tag{2.17}$$

$$dS = adE \tag{2.18}$$

where a is the slope and b is the intercept coefficients. Equation (2.16) can be written using Equations (2.17) and (2.18) as:

$$\rho x = \int_{S(E_{in})}^{S(E_{out})} \frac{1}{aS} dS = \left[\frac{1}{a} \ln S\right]_{S(E_{in})}^{S(E_{out})} = \frac{1}{a} \ln \frac{S(E_{out})}{S(E_{in})} \tag{2.19}$$

$$a\rho x = \ln\frac{S(E_{out})}{S(E_{in})} \tag{2.20}$$

$$S(E_{out}) = S(E_{in})e^{a\rho x} \tag{2.21}$$

The degraded energy of charged particles after passing through a thin foil can be calculated as follows.

$$E_{out} = E_{in}e^{a\rho x} + \frac{b}{a}(e^{a\rho x} - 1) \tag{2.22}$$

The energy degradations of a 50-MeV alpha-particle in the stacked targets (sets of V-Al-Ti-Ti-Al configuration) were calculated and shown in Fig. 2.5. The thicknesses of foils were calculated for ^{nat}V (25 µm), ^{nat}Ti (5 µm), and ^{27}Al (5 µm), respectively. Eleven sets of V-Al-Ti-Ti-Al foils were required to stop the alpha particles completely.

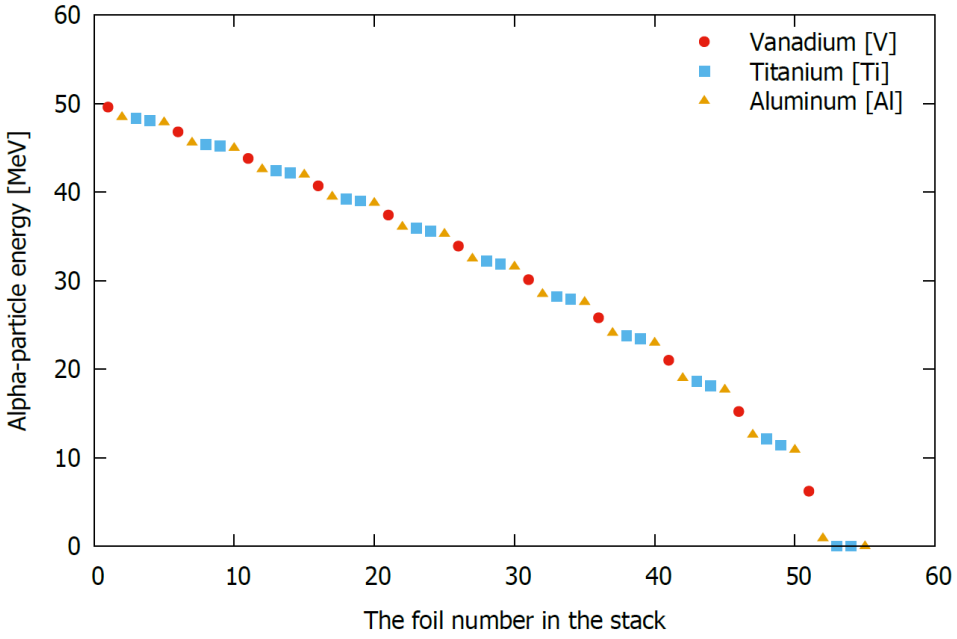

Fig. 2.5. Energy degradation of a 50-MeV alpha-particle beam in the stack target (V-Al-Ti-Ti-Al configuration)

2.2.2 Monitor reaction

The monitoring reactions are used to double-check the measured beam parameters and target thicknesses. The International Atomic Energy Agency (IAEA) publishes recommended values of several monitor reactions (Hermanne et al., 2018; Tárkányi et al., 2007) regarding the energy region

and projectile type. Charged-particle-induced monitor reactions are classified according to the projectile. The most common projectiles are protons, deuterons, ^{3}He-, and alpha-particles.

In our two experiments, the ^{nat}Ti(α,x)^{51}Cr and ^{nat}Ti(p,x)^{48}Cr monitor reactions were used, respectively. The monitor reactions and decay data of the activation products are listed in Table 2.1.

Table 2.1. Monitor reactions and decay data of the activation products

Reaction	Residual	Half-life	E_γ (keV)	I_γ (%)	Covered range (MeV)
^{nat}Ti(α,x)^{51}Cr	^{51}Cr	27.7010 d	320.082	9.91	8 – 45
^{nat}Ti(p,x)^{48}V	^{48}V	15.9735 d	983.525	99.98	5 – 100
			1312.105	98.2	

2.3 Gamma-ray spectrometry

High-resolution gamma-ray spectrometry is often used to measure the gamma-ray spectra of irradiated targets and monitor foils. The spectra can provide information about the radioactive isotopes present in the foils. This technique gives the precise identification and quantification of gamma-emitting isotopes. The high-purity germanium (HPGe) detector is one of the most used detectors in high-resolution gamma-ray spectrometry. This is due to its high efficiency, good energy resolution, and excellent sensitivity. The feature enables the detection of very low levels of gamma-emitting isotopes. The detectors are typically calibrated in energy scale and counting efficiency using standard gamma-ray sources. These calibrations are important for ensuring the accuracy and reliability of the results. The detector efficiency depends on the energy of the gamma rays and the distance between the radiation source and the detector.

The gamma-ray spectra of each irradiated foil are typically measured multiple times by an HPGe detector after an adequate cooling time. The gamma-ray spectra are analyzed by dedicated software. The net count of a peak in the gamma-ray spectra is proportional to the radioactivity of an isotope. The detector efficiency, branching ratio of the decay channels, and half-life of the isotope are important factors to calculate the activity of the isotope.

In our experiments, the gamma-ray spectra of each irradiated foil were measured by a high-resolution HPGe detector (ORTEC GEM-25185-P in Appendix B) and analyzed by the dedicated software (SEIKO EG&G Gamma Studio). The detector was calibrated by a multiple gamma-ray emitting point source consisting of ^{57,60}Co, ^{85}Sr, ^{88}Y, ^{109}Cd, ^{113}Sn ^{137}Cs, ^{139}Ce, ^{203}Hg, and ^{241}Am (Eckert & Ziegler Isotope Products in Appendix C and D). The distance between the detector and the foils was arranged to keep the dead time less than 5%.

CHAPTER 3: PRODUCTION CROSS SECTIONS OF ^{52G}MN IN ALPHA-PARTICLE-INDUCED REACTIONS ON NATURAL VANADIUM

3.1 Introduction

The radioisotope ^{52}Mn has the ground state ^{52g}Mn with a half-life of $T_{1/2}$ = 5.6 d, which decays via electron capture (70.6%) and positron emission (29.4%, $<E_{\beta+}>$ = 242 keV) processes. It has also a metastable state ^{52m}Mn ($T_{1/2}$ = 21.1 min) that decays to the ground state ^{52g}Mn by isomeric transition (IT) (1.8%) and ^{52}Cr by electron capture (1.6%) and positron emission (96.6%, $<E_{\beta+}>$ = 1172 keV) processes (National Nuclear Data Center, 2021). ^{52g}Mn can be used in Positron Emission Tomography (PET) imaging to study biological and physiological processes with a time scale similar to its decay (Bianchi et al., 2020).

The promising routes of the ^{52g}Mn production are proton- and deuteron-induced reactions on natural chromium or enriched ^{52}Cr targets (Tárkányi et al., 2019). Another possible production route is alpha-particle-induced reactions on natural vanadium (^{nat}V) targets. ^{nat}V is a monoisotopic element, although it has two isotopes of ^{51}V (stable, 99.75%) and ^{50}V ($T_{1/2} = 2.1\times10^{17}$ y, 0.25%) (National Nuclear Data Center, 2021). There are many previous measurements of alpha-particle-induced reactions on ^{nat}V (Ali et al., 2018; Bindu et al., 1998; Bowman & Blann, 1969; Chowdhury et al., 1995; Dmitriev et al., 1969; Hansper et al., 1993; Iguchi et al., 1960; Ismail, 1993; Levkovski, 1991; Michel et al., 1983; Neuzil & Lindsay, 1963; Peng et al., 1999; Rama et al., 1987; Singh et al., 1993, 1995; Sonzogni et al., 1993; Vlieks et al., 1974; Vonach et al., 1983). However, their data show large uncertainties and discrepancies.

In this chapter, we present the results of the excitation functions of the alpha-particle-induced reactions on ^{nat}V up to 50 MeV, with a particular focus on the ^{52g}Mn production. Activation cross sections of several co-produced radioisotopes were also determined. The experimental results were compared with earlier studies and theoretical calculations in the TENDL-2019 library (Koning et al., 2019). The physical yield of ^{52g}Mn was derived from the measured cross sections.

3.2 Experimental details

The experiment was performed at the AVF cyclotron of the RIKEN RI Beam Factory. The stacked-foil activation technique and high-resolution gamma-ray spectrometry were used.

3.2.1 Target preparation

The target for the experiment consisted of metallic foils of ^{nat}V (25-μm thick, 99% purity, Nilaco Corp., Japan), ^{nat}Ti (5-μm thick, 99.6% purity, Nilaco Corp., Japan), and ^{27}Al (5-μm thick, >99% purity, Nilaco Corp., Japan). The ^{27}Al foils were used to catch reaction products recoiled from the ^{nat}V and ^{nat}Ti foils. The ^{nat}Ti foils were interleaved for the ^{nat}Ti(α,x)^{51}Cr monitor reaction to assess beam parameters and target thicknesses. The target thicknesses were derived using measured sizes and weights of the foils. The derived thicknesses of the ^{nat}V, ^{nat}Ti, and ^{27}Al foils were 20.4, 2.24, and 1.22 mg/cm^2, respectively. The foils were cut into the size of 8×8 mm to fit into the target holder, which served as a Faraday cup. The target configuration of three types of foils was arranged based on the calculations of energy degradation. Eleven sets of V-Al-Ti-Ti-Al foils (Fig. 3.1) were stacked in the target holder.

Fig. 3.1. The target configuration (^{nat}V, ^{nat}Ti, and ^{27}Al foils)

3.2.2 Irradiation

The stacked target was irradiated for 30 minutes with a 50.6±0.2 MeV alpha-particle beam. The primary beam energy was measured by the time-of-flight method (Watanabe et al., 2014). The energy degradation in the stacked target was calculated using the target thicknesses and stopping powers

derived from the SRIM code (Ziegler et al., 2010). The average beam intensity measured by the Faraday cup was 194 nA.

3.2.3 Activity measurement

The gamma-ray spectra of each irradiated foil were measured without chemical separation by a high-resolution HPGe detector (ORTEC GEM-25185-P). The gamma-ray spectra were analyzed by the dedicated software (SEIKO EG&G Gamma Studio). The detector was calibrated by a multiple gamma-ray emitting point source consisting of ^{57,60}Co, ^{88}Y, ^{109}Cd, ^{113}Sn ^{137}Cs, ^{139}Ce, and ^{241}Am. Each ^{nat}V foil was measured together with the next ^{27}Al catcher foil of recoiled products. Each foil was measured three times in 17 days to follow the decay of the produced radioisotopes with different half-lives. The distance between the detector and the foils was arranged to keep the dead time less than 3%.

Table 3.1. Measurement conditions

Series	Cooling time	Distance (cm)	Dead time (%)
Ser. 1 (^{nat}V)	1.6-6.2 h	1-15	0.1-2.1
Ser. 2 (^{nat}V)	6.5-50 h	1-15	<1.7
Ser. 3 (^{nat}V)	15-17 d	5	<1.7

3.2.4 Nuclear reaction and decay data

The nuclear reaction and decay data for the gamma-ray spectrometry were taken from NuDat 3.0 (National Nuclear Data Center, 2021), LiveChart (International Atomic Energy Agency, 2009), Lund/LBNL Nuclear Data Search (Chu et al., 1999), and QCalc (Sonzogni & Pritychenko, 2003). Reaction and decay data for the radionuclides of interest are listed in Table 3.2.

Table 3.2. Reactions and decay data of reaction products.

Nuclide	Half-life	Decay mode (%)	E_γ (keV)	I_γ (%)	Contributing reactions	Q-value (MeV)
^{54}Mn	312.20 d	ε (100)	**834.848**	99.976(10)	^{50}V(α, γ)^{54}Mn	8.8
					^{51}V(α, n)^{54}Mn	-2.3
^{52g}Mn	5.591 d	ε + β^+ (100)	744.233	90(12)	^{50}V(α, 2n)^{52}Mn	-12.2
			935.544	94.5(13)	^{51}V(α, 3n)^{52}Mn	-23.3
			1434.092	100(14)		
^{51}Cr	27.7025 d	ε (100)	**320.0824**	9.91(10)	^{50}V(α, t)^{51}Cr	-10.3
					^{51}V(α, tn)^{51}Cr	-21.3
^{51}Mn	46.2 m	ε + β^+ (100)	511.0	194.18(6)	^{50}V(α, 3n)^{51}Mn	-22.8

			749.07	0.265	^{51}V(α, 4n)^{51}Mn	-33.8
^{48}V	15.9735 d	ε + β^+ (100)	**983.525**	99.98(4)	^{50}V(α, α2n)^{48}V	-20.9
			1312.106	98.2(3)	^{51}V(α, α3n)^{48}V	-31.9
^{48}Sc	43.67 h	β^- (100)	983.526	100.1(6)	^{50}V(α, α2p)^{48}Sc	-19.3
			1037.522	97.6(7)	^{51}V(α, α^{3}He)^{48}Sc	-22.6
			1312.12	100.1(7)		
^{48}Cr	21.56 h	ε (100)	112.31	96(20)	^{50}V(α, t3n)^{48}Cr	-43.1
			308.24	100		
^{47}Sc	3.3492 d	β^- (100)	**159.381**	68.3(4)	^{50}V(α, α^{3}He)^{47}Sc	-10.3
					^{51}V(α, 2α)^{47}Sc	-19.8
^{47}Ca	4.536 d	β^- (100)	807.86	5.9(12)	^{50}V(α, α3p)^{47}Ca	-28.7
			1297.09	67	^{51}V(α, αp^{3}He)^{47}Ca	-32.1
^{46g}Sc	83.79 d	β^- (100)	**889.277**	99.984(10)	^{50}V(α, 2α)^{46}Sc	-9.9
			1120.545	99.987(10)	^{51}V(α, 2αn)^{46}Sc	-20.1
^{51}Cr	27.7025 d	ε (100)	**320.0824**	9.91(10)	^{nat}Ti(α, x)^{51}Cr	

3.2.5 Monitor reaction

Cross sections of the ^{nat}Ti(α,x)^{51}Cr monitor reaction were derived to assess the beam parameters and target thicknesses. The gamma line at 320.08 keV (I_γ = 9.91%) from the decay of ^{51}Cr ($T_{1/2}$ = 27.7025 d) was measured. Only the second Ti foil of each Ti-Ti foil pair in the stack was assessed, as their recoiled ^{51}Cr were considered to be compensated by the first foils. The dead time during the measurements was kept less than 1% after a cooling time of 3 days.

The derived cross sections were compared with the IAEA recommended values (Hermanne et al., 2018; Tárkányi et al., 2007) as shown in Fig. 3.2. Our result is consistent with the recommended values published in 2007. The measured thicknesses and beam parameters were used without any correction to derive production cross sections.

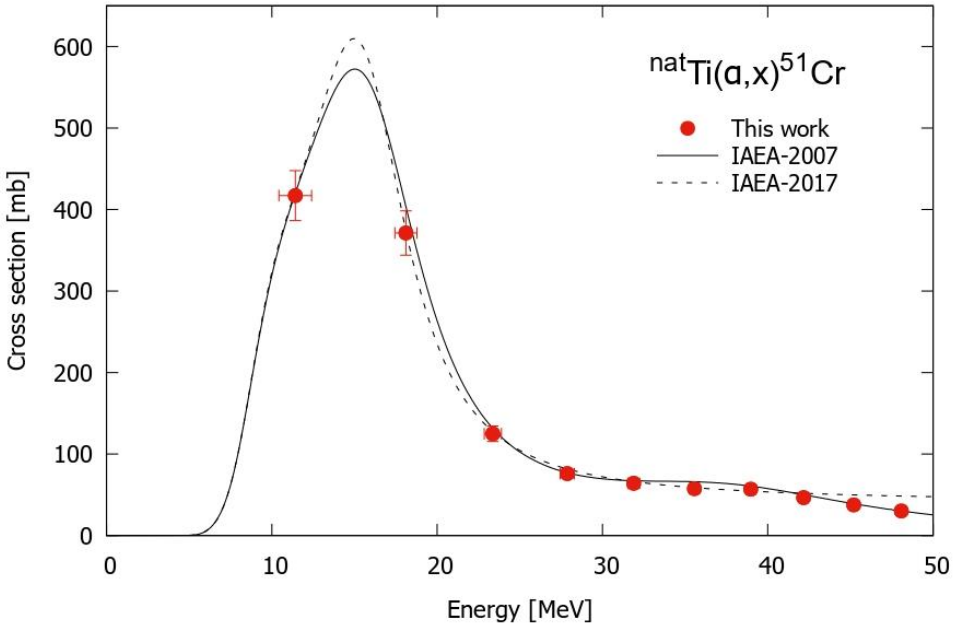

Fig. 3.2. Excitation function of the $^{nat}Ti(\alpha,x)^{51}Cr$ monitor reaction with the recommended values (Hermanne et al., 2018; Tárkányi et al., 2007).

3.3 Result and discussion

The activation cross sections of $^{54, 52g}$Mn, ^{51}Cr, ^{48}V, and $^{47, 46g}$Sc were determined for the alpha-particle-induced reactions on ^{nat}V. The numerical data of the measured cross sections are listed in Table 3.3. The results are displayed in Figs. 3.3-3.8 together with the previous experimental studies and the TENDL-2019 data. The production yield of ^{52g}Mn deduced from the measured cross sections is shown in Fig. 3.9. The yield was compared with the previous experimental data (Dmitriev et al., 1969).

The median projectile energy at each foil is listed in Table 3.3 with the total uncertainty and energy loss in parathesis. The total energy uncertainties of 0.2-1.3 MeV were propagated from the uncertainties of the primary beam energy (±0.2 MeV) and target thickness (1%). The estimated energy loss in the ^{nat}V foils was 1.0-5.3 MeV. The total uncertainty of the cross sections was estimated to be 7.2-29.5%. It was derived from the square root of the quadratic summation of each component; beam intensity (5%), gamma-line intensity (<13%), detector efficiency (5%), target thickness (1%), target purity (1%), and counting statistics (0.2-28.6%).

Table 3.3. Measured production cross sections (mb).

Energy (MeV)	^{54}Mn	^{52g}Mn(cum)	^{51}Cr(cum)	^{48}V(cum)	^{47}Sc	^{46g}Sc(cum)
49.6±0.2 (±1.0)	6.09±0.59	145±10	296±22	9.69±0.70	3.89±0.31	12.1±0.9
46.8±0.2 (±1.1)	6.99±1.13	190±14	194±14	2.14±0.20	4.17±0.35	7.23±0.63
43.8±0.2 (±1.1)	8.89±1.31	230±17	95.5±7.1	0.507±0.108	4.80±0.39	3.18±0.40
40.7±0.3 (±1.2)	11.9±1.5	259±19	33.8±2.8		4.49±0.37	
37.4±0.3 (±1.2)	13.0±1.5	239±17	9.68±1.38		2.66±0.26	
33.9±0.3 (±1.3)	16.6±1.6	172±12	4.73±1.06		1.45±0.20	
30.1±0.4 (±1.5)	25.5±2.0	59.2±4.3	2.11±0.62		0.433±0.102	
25.8±0.5 (±1.6)	47.0±3.5	2.03±0.16			0.0267±0.0027	
21.0±0.6 (±1.9)	150±11	0.889±0.081				
15.1±0.8 (±2.4)	554±40	0.187±0.030				
6.5±1.8 (±4.1)	111±8					

3.3.1 The ^{nat}V(α,x)^{54}Mn reaction

The cross sections of the ^{nat}V(α,x)^{54}Mn reaction were derived from net counts of the gamma line at 834.848 keV (I_γ = 99.976%) emitted with the decay of ^{54}Mn ($T_{1/2}$ = 312.20 d). The gamma line was measured after an average cooling time of 17 days.

The result is compared with the previous studies (Ali et al., 2018; Bindu et al., 1998; Bowman & Blann, 1969; Chowdhury et al., 1995; Hansper et al., 1993; Iguchi et al., 1960; Ismail, 1993;

Levkovski, 1991; Michel et al., 1983; Peng et al., 1999; Rama et al., 1987; Singh et al., 1993, 1995; Sonzogni et al., 1993; Vlieks et al., 1974; Vonach et al., 1983) and the TENDL-2019 data (Koning et al., 2019) as shown in Fig. 3.3. Our data point at the lowest energy is shifted to the lower energy region because the beam was fully stopped at the corresponding foil.

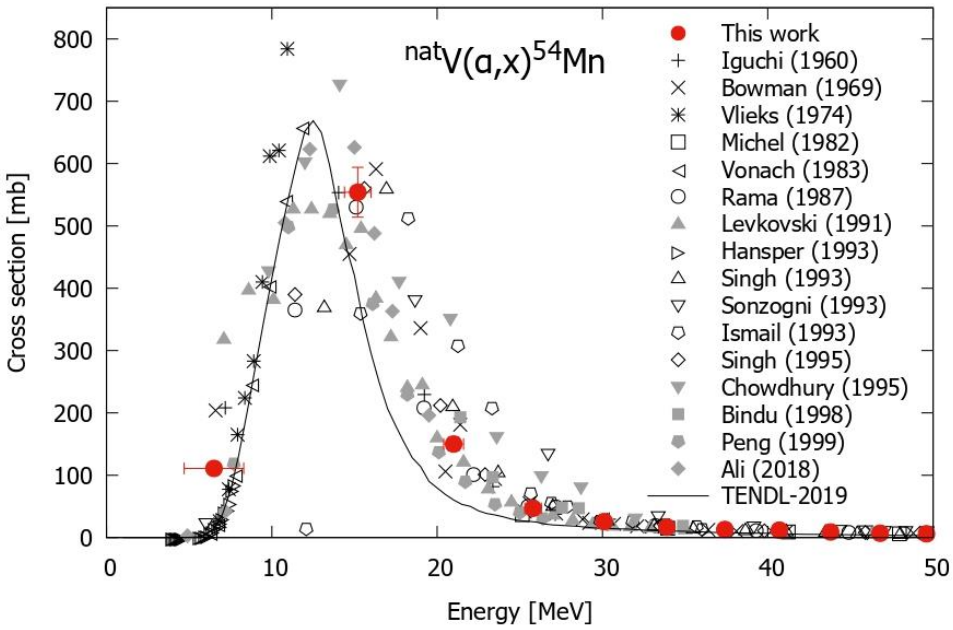

Fig. 3.3. Excitation function of the $^{nat}V(\alpha,x)^{54}Mn$ reaction.

The present data are consistent with the data of Ali et al. (2018), Bindu et al. (1998), Bowman & Blann (1969), Iguchi et al. (1960), Levkovski (1991), Michel et al. (1983), Peng et al. (1999), and Sonzogni et al. (1993). Partial agreement is found with the data of Chowdhury et al. (1995), Ismail (1993), Rama et al. (1987), and Singh et al. (1993, 1995) in the higher energy region. The data below 11 MeV by Hansper et al. (1993), Vlieks et al. (1974), and Vonach et al. (1983) are smaller than ours, while the previous data are consistent with each other except for part of the data by Vlieks et al. (1974) at around the peak. The TENDL-2019 data show the same trend as the experimental excitation function while they underestimate the peak amplitude.

3.3.2 The $^{nat}V(\alpha,x)^{52g}Mn$ reaction

The cross sections of the $^{nat}V(\alpha,x)^{52g}Mn$ reaction were derived. The radionuclide ^{52}Mn has a short-lived metastable state ($T_{1/2}$ = 21.1 min), which decays partially to the ground state ^{52g}Mn ($T_{1/2}$ = 5.591 d), and the stable ^{52}Cr soon after the end of the bombardment. The gamma line at 935.544 keV (I_γ = 94.5%) from the decay of ^{52g}Mn was measured after a cooling time of 17 days. The cumulative cross sections were obtained from the net counts of the gamma peak.

The derived cross sections are shown in Fig. 3.4 and compared with the previous studies (Bindu et al., 1998; Bowman & Blann, 1969; Chowdhury et al., 1995; Dmitriev et al., 1969; Ismail, 1993; Levkovski, 1991; Michel et al., 1983; Rama et al., 1987; Singh et al., 1993, 1995; Sonzogni et al., 1993) and the TENDL-2019 data (Koning et al., 2019).

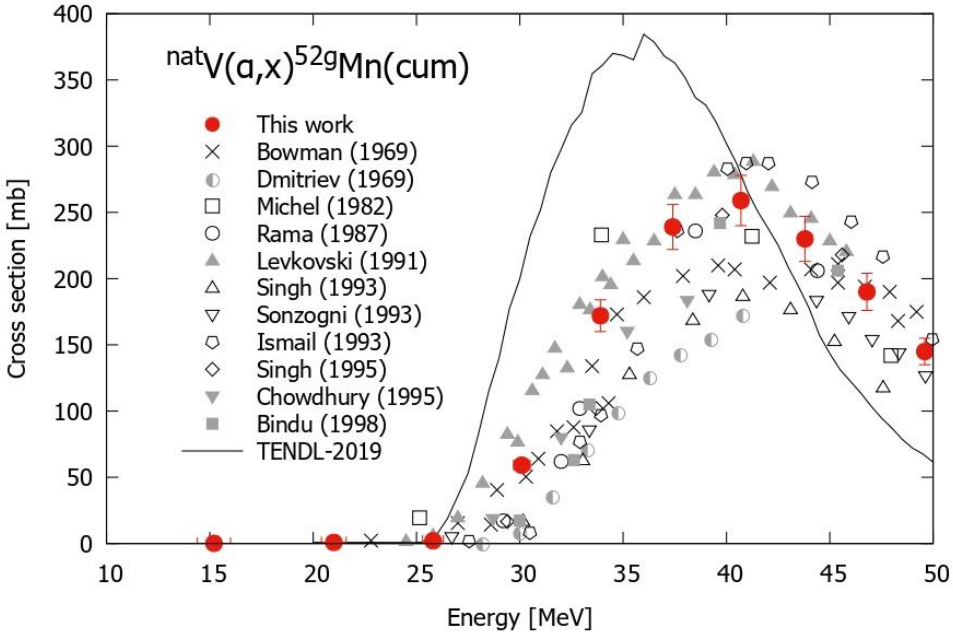

Fig. 3.4. Excitation function of the $^{nat}V(\alpha,x)^{52g}Mn$ reaction.

The present cross-section data show a smooth curve and are consistent with part of the previous experimental data. The data reported by Levkovski (1991) agree with our data. The experimental data of Bindu et al. (1998), Bowman & Blann (1969), Ismail (1993), Michel et al. (1983), and Singh et al. (1995) are in partial agreement with our data. The data of Chowdhury et al. (1995), Dmitriev et al. (1969), Rama et al. (1987), Singh et al. (1993), and Sonzogni et al. (1993) are lower than ours. The peak position and amplitude of the TENDL-2019 data are different from the experimental data.

3.3.3 The $^{nat}V(\alpha,x)^{51}Cr$ reaction

Measurements of the 320.08-keV gamma line (I_γ = 9.91%) after a cooling time longer than 17 days were used to derive the production cross sections of ^{51}Cr ($T_{1/2}$ = 27.7025 d). Its parent ^{51}Mn ($T_{1/2}$ = 46.2 min) decayed completely during the cooling time.

The cumulative cross sections are shown in Fig. 3.5 together with the previous experimental data (Bowman & Blann, 1969; Chowdhury et al., 1995; Ismail, 1993; Levkovski, 1991; Michel et al., 1983; Singh et al., 1993, 1995; Sonzogni et al., 1993) and the TENDL-2019 data (Koning et al., 2019).

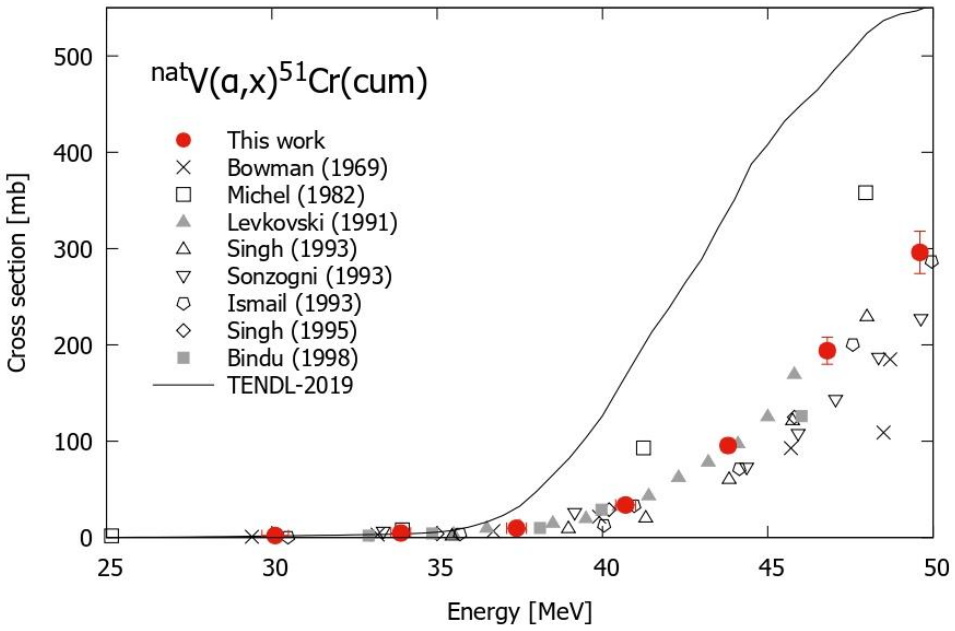

Fig. 3.5. Excitation function of the $^{nat}V(\alpha,x)^{51}Cr$ reaction.

The present cross sections are consistent with the data reported by Bindu et al. (1998), Ismail (1993), Levkovski (1991), and Singh et al. (1993, 1995). Both datasets of Bowman & Blann (1969), and Sonzogni et al. (1993) are slightly lower than ours in the higher energy region. The data reported by Michel et al. (1982) is higher than the other experimental data. The TENDL-2019 data are larger than all the experimental data above 35 MeV.

3.3.4 The $^{nat}V(\alpha,x)^{48}V$ reaction

The excitation function of the $^{nat}V(\alpha,x)^{48}V$ reaction was derived from measurements of the gamma line at 983.525 keV (I_γ = 99.98%) from the ^{48}V decay ($T_{1/2}$ = 15.9735 d). The measurements were performed after an average cooling time of 17 days. During the cooling time, the parent nucleus ^{48}Cr ($T_{1/2}$ = 21.56 h) decayed to ^{48}V. The possible contribution of ^{48}Sc ($T_{1/2}$ = 43.67 h) to the gamma line was negligible because another gamma line at 1037.522 keV (I_γ = 97.6%) from the ^{48}Sc decay could not be found in the spectra.

The cumulative cross sections are shown in Fig. 3.6 together with the experimental data studied earlier (Bindu et al., 1998; Ismail, 1993; Michel et al., 1983; Singh et al., 1993, 1995; Sonzogni et al., 1993) and the TENDL-2019 data (Koning et al., 2019).

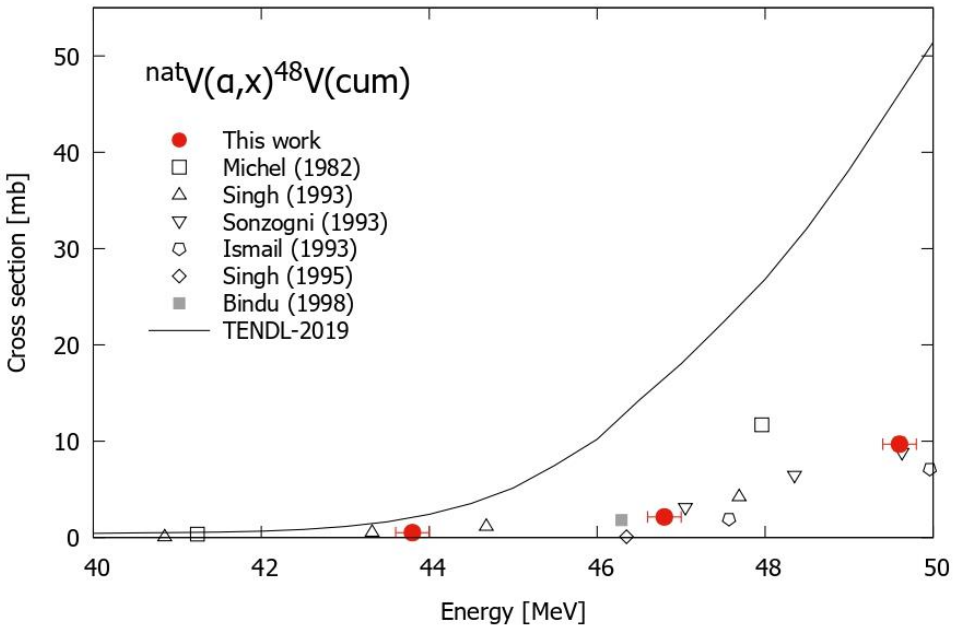

Fig. 3.6. Excitation function of the $^{nat}V(\alpha,x)^{48}V$ cumulative reaction.

The present data are consistent with the data of Singh et al. (1993), Sonzogni et al. (1993), and Bindu et al. (1998) within uncertainty. The data of Ismail (1993), and Singh et al. (1995) are lower than ours while the data reported by Michel et al. (1983) are higher than the other experimental data. The TENDL-2019 data overestimate the experimental cross sections.

3.3.5 The $^{nat}V(\alpha,x)^{47}Sc$ reaction

The production cross sections of ^{47}Sc ($T_{1/2}$ = 3.3492 d) were derived from the gamma line at 159.381 keV (I_γ = 68.3%). We used the gamma spectra recorded after a cooling time of 1 day. The formation of ^{47}Ca ($T_{1/2}$ = 4.536 d) was energetically possible but negligible because the gamma line at 1297.09 keV (I_γ = 67%) from ^{47}Ca decay could not be found in the spectra.

The cross sections are shown in Fig. 3.7 together with the previous experimental data (Bindu et al., 1998; Bowman & Blann, 1969; Ismail, 1993; Levkovski, 1991; Michel et al., 1983; Neuzil & Lindsay, 1963; Singh et al., 1993, 1995; Sonzogni et al., 1993) and the TENDL-2019 data (Koning et al., 2019).

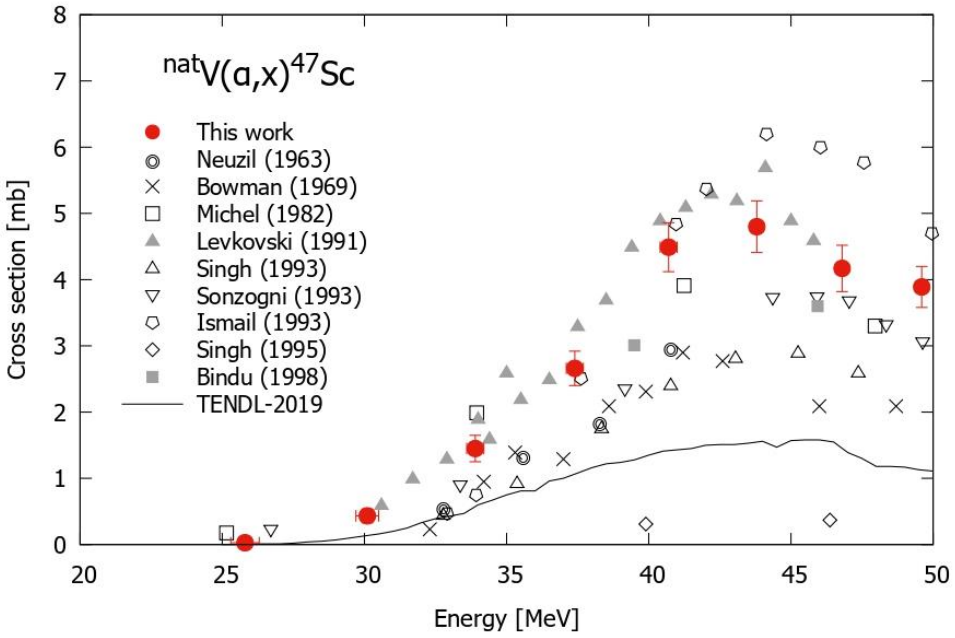

Fig. 3.7. Excitation function of the $^{nat}V(\alpha,x)^{47}Sc$ reaction.

Our result is consistent with the data of Levkovski (1991). The experimental data of Ismail (1993), and Michel et al. (1983) are in partial agreement with ours. The data of Bindu et al. (1998), Bowman & Blann (1969), Neuzil & Lindsay (1963), Singh et al. (1993, 1995), and Sonzogni et al. (1993) are lower than our data. The TENDL-2019 data underestimate the experimental values except for the data of Singh (1995).

3.3.6 The $^{nat}V(\alpha,x)^{46g}Sc$ reaction

The cross sections for the ^{46g}Sc production were derived by measuring the 889.277-keV gamma line (I_γ = 99.984%) from the decay ($T_{1/2}$ = 83.79 d). The metastable state ^{46m}Sc has a short half-life ($T_{1/2}$ = 18.75 s, IT: 100%) and decayed to ^{46g}Sc during the irradiation. The measurements of the gamma line were performed after an average cooling time of 17 days.

The cumulative cross sections are shown in Fig. 3.8 together with the previous experimental data (Bindu et al., 1998; Bowman & Blann, 1969; Ismail, 1993; Levkovski, 1991; Michel et al., 1983; Neuzil & Lindsay, 1963; Singh et al., 1995; Sonzogni et al., 1993) and the TENDL-2019 data (Koning et al., 2019).

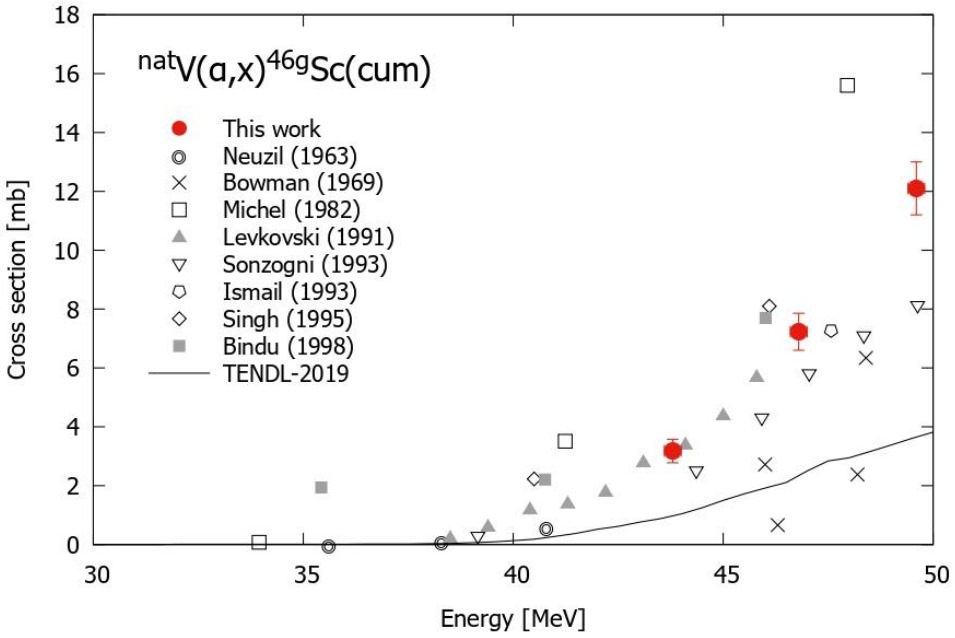

Fig. 3.8. Excitation function of the $^{nat}V(\alpha,x)^{46g}Sc$ reaction.

The data of Ismail (1993), Levkovski (1991), and Neuzil & Lindsay (1963) are nearly consistent with our data. The data of Bindu et al. (1998), Michel et al. (1983), and Singh et al. (1993) are higher than our results. The data of Bowman & Blann (1969) and Sonzogni et al. (1993) are lower than ours. The TENDL-2019 data underestimate the experimental data other than part data of Bowman & Blann (1969).

3.3.7 The physical yield of ^{52g}Mn

Physical thick target yield (Otuka & Takács, 2015) of ^{52g}Mn was deduced up to 49.6 MeV from the spline fitted curve of the measured excitation function of the $^{nat}V(\alpha,x)^{52g}Mn$ reaction in section 3.2 and stopping powers calculated using the SRIM code (Ziegler et al., 2010).

The physical yield is displayed in Fig. 3.9 together with the previously published experimental data (Dmitriev et al., 1969). Our result is higher than the previous data, which can be expected from the difference in the cross sections shown in Fig. 3.4.

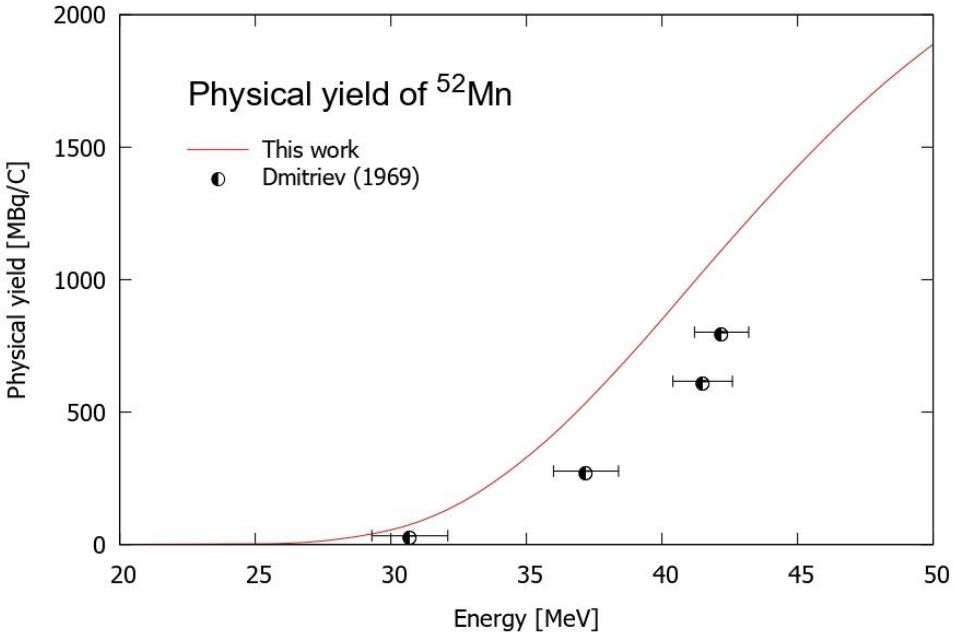

Fig. 3.9. Physical yield of ^{52g}Mn in the alpha-particle-induced reaction on ^{nat}V.

3.4 Summary

We measured excitation functions of the alpha-particle-induced reactions on ^{nat}V up to 50 MeV at the RIKEN AVF cyclotron. The production cross sections of ^{52g}Mn and co-produced ^{54}Mn, ^{51}Cr, ^{48}V, and $^{47,\ 46g}$Sc were determined. The stacked-foil activation technique and the high-resolution gamma-ray spectrometry were used for the cross-section measurements.

The measured data are compared with previous experimental data and the theoretical calculations in the TENDL-2019 library. The derived excitation function of the ^{nat}V(α,x)^{52g}Mn reaction is consistent with the earlier published data by Levkovski (1991). The physical yield of ^{52g}Mn deduced from the measured cross sections is larger than the experimental data of Dmitriev et al. (1969).

CHAPTER 4: PRODUCTION CROSS SECTIONS OF ^{198G}AU IN PROTON-INDUCED REACTIONS ON NATURAL PLATINUM

4.1 Introduction

Gold-198 has two long-lived states, the ground state ^{198g}Au ($T_{1/2}$ = 2.6941 d) and the metastable state ^{198m}Au ($T_{1/2}$ = 2.272 d) that decays to the ground state by the isomeric transition (IT: 100%). The radionuclide ^{198g}Au is a beta emitter (β^-: 100%, $<E_{\beta^-}>$ = 312.5 keV) and is widely used for therapy in nuclear medicine, such as brachytherapy (Fernandes et al., 2003; Horiuchi et al., 1991; Karvat et al., 2001; Konishi et al., 2021) and nanoparticles (Black et al., 2014; Chakravarty et al., 2019; Chanda et al., 2010).

The large-scale production route of ^{198g}Au is the neutron capture reaction on monoisotopic element ^{197}Au in nuclear reactors. The route, however, can produce only the low specific activity of ^{198g}Au because of the difficult chemical separation from the ^{197}Au target. The high specific activity ^{198g}Au can be produced using cyclotrons with proton- and deuteron-induced reactions on natural and enriched platinum targets.

In this chapter, we focused on the proton-induced reactions on ^{nat}Pt targets (^{190}Pt: 0.012%, ^{192}Pt: 0.782%, ^{194}Pt: 32.864%, ^{195}Pt: 33.775%, ^{196}Pt: 25.211%, and ^{198}Pt: 7.356%) (Meija et al., 2016). Four previous experimental studies (Showaimy et al., 2019; Smith et al., 2017; Tárkányi et al., 2004a, 2004b) for isotope production by proton-induced reactions on platinum were found in our literature survey. The previous experimental cross-section data have large uncertainties and show discrepancies among them. More reliable and accurate data are required. Therefore, we measured the excitation functions of the proton-induced reactions on ^{nat}Pt up to 30 MeV, with a particular focus on the ^{198g}Au production. Activation cross sections of several co-produced radioisotopes were also determined. The results were compared with the experimental data published earlier (Showaimy et al., 2019; Tárkányi et al., 2004a, 2004b) and the TENDL-2019 data based on a calculation using the theoretical model code TALYS (Koning et al., 2019).

4.2 Experimental details

The experiment was performed at the AVF cyclotron of the RIKEN RI Beam Factory. The stacked-foil activation technique and high-resolution gamma-ray spectrometry were used.

4.2.1 Target preparation

The target for the experiment consisted of pure metallic foils of ^{nat}Pt (20-μm thick, 99.95% purity, 100×100 mm size), and ^{nat}Ti (5-μm thick, 99.6% purity, 50×100 mm size), which were purchased from Nilaco Corp., Japan. The ^{nat}Ti foils were used for the ^{nat}Ti(p,x)^{48}V monitor reaction to assess the beam parameters and the target thicknesses. The target thicknesses were derived using measured sizes and weights of the foils. The derived thicknesses of the ^{nat}Pt and ^{nat}Ti foils were 39.2, and 2.24 mg/cm^2, respectively. The foils were cut into the size of 10×10 mm to fit into the target holder, which served as a Faraday cup. The target configuration of two types of foils was arranged based on the calculations of energy degradation. Twenty-five sets of Pt-Pt-Ti-Ti foils as shown in Fig. 4.1 were stacked in the target holder.

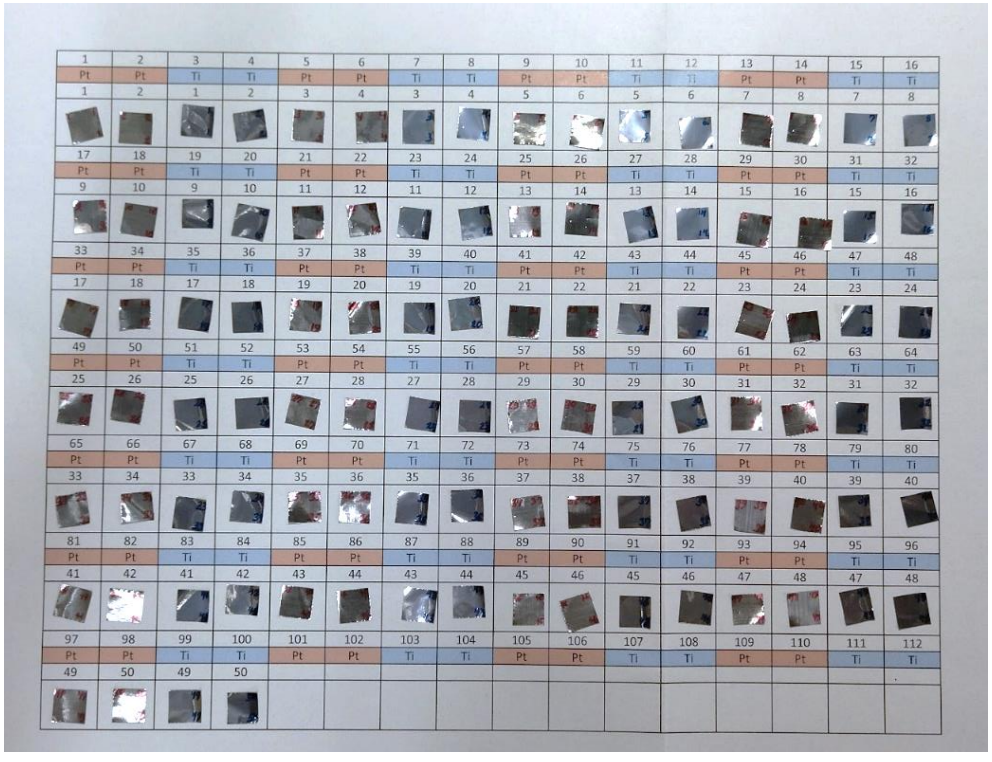

Fig. 4.1. The target configuration (^{nat}Pt and ^{nat}Ti foils)

4.2.2 Irradiation

The stacked target was irradiated for 30 minutes with a 30.1±0.1 MeV proton beam. The primary beam energy was measured by the time-of-flight method (Watanabe et al., 2014). The energy degradation in the stacked target was calculated using the target thicknesses and stopping powers derived using the SRIM code (Ziegler et al., 2010). The average beam intensity measured by the Faraday cup was 101 nA.

4.2.3 Activity measurement

The gamma-ray spectra of each irradiated foil were measured without chemical separation by a high-resolution HPGe detector (ORTEC GEM-25185-P). The gamma-ray spectra were analyzed by the dedicated software (SEIKO EG&G Gamma Studio). The detector was calibrated by a multiple gamma-ray emitting point source consisting of ^{57,60}Co, ^{85}Sr, ^{88}Y, ^{109}Cd, ^{113}Sn ^{137}Cs, ^{139}Ce, ^{203}Hg, and ^{241}Am (Eckert & Ziegler Isotope Products). Every second foil of the same element pairs was measured assuming compensation for the recoil losses of the products. Each foil was measured four times in 2 hours - 70 days to follow the decay of the produced radioisotopes with different half-lives. The distance between the detector and the foils was arranged to keep the dead time less than 4.7%.

Table 4.1. Measurement conditions

Series	Cooling time	Distance (cm)	Dead time (%)
Ser. 1 (^{nat}Pt)	2.3 – 11 h	20 – 100	0.1 – 4.7
Ser. 2 (^{nat}Pt)	22 – 34 h	20 – 50	0.1 – 3.2
Ser. 3 (^{nat}Pt)	13 – 15 d	5	<1.1
Ser. 4 (^{nat}Pt)	68 – 70 d	2	<0.4

4.2.4 Nuclear reaction and decay data

The nuclear reaction and decay data for the gamma-ray spectrometry were taken from NuDat 3.0 (National Nuclear Data Center, 2021), LiveChart (International Atomic Energy Agency, 2009b), Lund/LBNL Nuclear Data Search (Chu et al., 1999), and QCalc (A. Sonzogni & Pritychenko, 2003). Reaction and decay data for the radionuclides of interest are listed in Table 4.2.

Table 4.2. Reactions and decay data of reaction products.

Nuclide	Half-life	Decay mode (%)	E_γ (keV)	I_γ (%)	Contributing reaction	Q-value (MeV)
^{198g}Au	2.6941 d	β^- (100)	**411.80205**	95.62(6)	^{198}Pt(p,n)^{198g}Au	-1.1
^{196g}Au	6.1669 d	β^- (7)	333.03	22.9(9)	^{198}Pt(p,3n)^{196g}Au	-15.7

		ε+β^+ (93)	**355.73**	87(3)	^{196}Pt(p,n)^{196g}Au	-2.3
					^{195}Pt(p,γ)^{196g}Au	5.6
^{196m2}Au	9.6 h	IT (100)	**147.81**	43.5(15)	^{198}Pt(p,3n)^{196m2}Au	-16.3
			188.27	30.0(15)	^{196}Pt(p,n)^{196m2}Au	-2.9
					^{195}Pt(p,γ)^{196m2}Au	5.0
^{195g}Au	186.01 d	ε (100)	**98.857**	11.21(15)	^{198}Pt(p,4n)^{195g}Au	-22.3
					^{196}Pt(p,2n)^{195g}Au	-8.9
					^{195}Pt(p,n)^{195g}Au	-1.0
					^{194}Pt(p,γ)^{195g}Au	5.1
^{194g}Au	38.02 h	ε+β^+ (100)	293.549	10.9(3)	^{196}Pt(p,3n)^{194g}Au	-17.4
			328.470	62.8(16)	^{195}Pt(p,2n)^{194g}Au	-9.4
			1468.904	6.8(20)	^{194}Pt(p,n)^{194g}Au	-3.3
^{193g}Au	17.65 h	ε+β^+ (100)	112.515	2.2(3)	^{196}Pt(p,4n)^{193g}Au	-24.2
			173.52	2.8	^{195}Pt(p,3n)^{193g}Au	-16.3
			186.17	9.7(11)	^{194}Pt(p,2n)^{193g}Au	-10.2
			255.57	6.5(9)	^{192}Pt(p,γ)^{193g}Au	4.4
			268.22	3.8(5)		
			439.04	1.85(23)		
^{192g}Au	4.94 h	ε+β^+ (100)	295.95650	23(3)	^{195}Pt(p,4n)^{192g}Au	-25.0
			316.50618	59(7)	^{194}Pt(p,3n)^{192g}Au	-18.9
					^{192}Pt(p,n)^{192g}Au	-4.3
^{191g}Au	3.18 h	ε+β^+ (100)	**586.44**	15.0	^{194}Pt(p,4n)^{191g}Au	-26.0
					^{192}Pt(p,2n)^{191g}Au	-11.3
					^{190}Pt(p,γ)^{191g}Au	3.8
^{191}Pt	2.83 d	ε (100)	**538.87**	14.3(24)	^{196}Pt(p,t3n)^{191}Pt	-28.8
					^{195}Pt(p,t2n)^{191}Pt	-20.9
					^{194}Pt(p,tn)^{191}Pt	-14.8
					^{192}Pt(p,d)^{191}Pt	-6.4
					^{191}Au decay	
^{192g}Ir	73.829 d	ε (4.76)	295.95650	28.71(7)	^{198}Pt(p,α3n)^{192g}Ir	-14.4
		β^- (95.24)	308.45507	29.70(7)	^{196}Pt(p,αn)^{192g}Ir	-1.0
			316.50618	82.86(3)	^{195}Pt(p,α)^{192g}Ir	6.9
			468.06885	47.84(3)	^{194}Pt(p,^{3}He)^{192g}Ir	-7.6
^{190g}Ir	11.78 d	ε+β^+ (100)	**186.68**	50(3)	^{196}Pt(p,α3n)^{190g}Ir	-15.2
			361.09	12.3(5)	^{195}Pt(p,α2n)^{190g}Ir	-7.3
			371.24	21.6(7)	^{194}Pt(p,αn)^{190g}Ir	-1.2
			407.22	22.7(13)	^{192}Pt(p,^{3}He)^{190g}Ir	-7.2
			518.55	32.2(15)		

				557.95	28.5(13)	
				569.30	27.0(12)	
				605.14	37.8(18)	
^{48}V	15.9735 d	ε (100)		**983.525**	99.98	^{nat}Ti(p,x)^{48}V
				1312.105	98.2	

The self-absorption of low-energy gamma lines in the Pt foils was considered using the following equation (Alfassi et al., 2009):

$$A(E) = A_0(E)\frac{\rho[\mu(E)/\rho]d}{1 - exp\,[-\rho(\mu(E)/\rho)d]} \quad (4.1)$$

where $A_0(E)$ is the measured activity for the gamma line at the energy E, $A(E)$ is the corrected activity, d is the thickness of the Pt foil, ρ is the density of the foil, $\mu(E)/\rho$ is the mass attenuation coefficient for the gamma line at the energy. The mass attenuation coefficient was taken from the online database (Hubbel & Seltzer, 2004).

4.2.5 Monitor reaction

Cross sections of the ^{nat}Ti(p,x)^{48}V monitor reaction were derived to assess the beam parameters and target thicknesses. The gamma line at 983.5 keV (I_γ = 99.98%) from the decay of ^{48}V ($T_{1/2}$ = 15.9735 d) in each second Ti foil was measured. The dead time during the measurements was kept less than 0.3% after a cooling time of 2 days. The possible contribution from ^{48}Sc ($T_{1/2}$ = 43.67 h) in the spectra was negligible because production cross sections of ^{48}Sc are tiny in this energy region and the 1037.52-keV gamma line from ^{48}Sc was not found in the spectra.

The derived cross sections were compared with the IAEA recommended values (Hermanne et al., 2018; Tárkányi et al., 2007) as shown in Fig. 4.2. Our result is consistent with the recommended values published in 2007. The measured thicknesses and beam parameters were used without any correction to derive production cross sections.

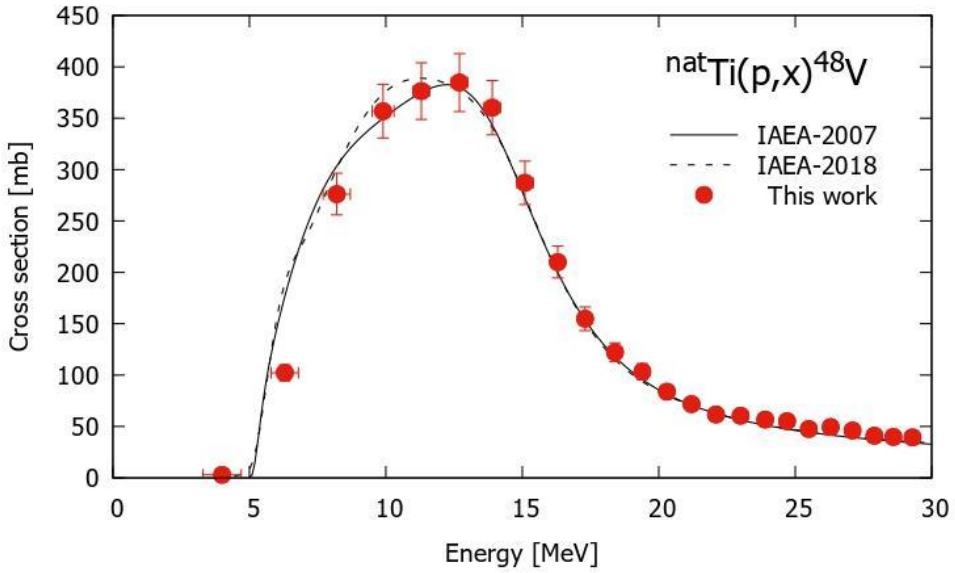

Fig. 4.2. Excitation function of the $^{nat}Ti(p,x)^{48}V$ monitor reaction with the recommended values (Hermanne et al., 2018; Tárkányi et al., 2007).

4.3 Result and discussion

The activation cross sections of $^{198, 196, 196m2, 195, 194, 193, 192, 191}$Au, ^{191}Pt, and $^{192, 190}$Ir were determined for the proton-induced reactions on ^{nat}Pt up to 30 MeV. The numerical data of the measured cross sections are listed in Tables 2 and 3. The results are displayed in Figs. 4.3-4.13 together with the previous experimental studies (Showaimy et al., 2019; Tárkányi et al., 2004a, 2004b) and the TENDL-2019 data (Koning et al., 2019). The TENDL-2019 data shown in each figure were normalized to the natural isotopic ratio and appropriately summed up for independent or cumulative elemental cross sections for comparison.

The median projectile energy at each foil is listed in Tables 4.3 and 4.4 with the total uncertainty and energy loss in parathesis. The total energy uncertainties of 0.1-0.7 MeV were propagated from the uncertainties of the primary beam energy (±0.1 MeV) and target thickness (1%). The estimated energy loss in the ^{nat}Pt foils was 0.2-0.6 MeV. The total uncertainty of the cross sections was estimated to be 7.2-29.9%. It was derived from the square root of the quadratic summation of each component; beam intensity (5%), gamma-line intensity (<17%), detector efficiency (5%), target thickness (1%), target purity (1%), and counting statistics (0.3-28.7%).

Table 4.3. Measured cross sections of $^{198, 196, 196m2, 195, 194}$Au in the ^{nat}Pt(p,x) reaction. The projectile energy is listed with total uncertainty and energy loss in parathesis.

E (MeV)	^{198g}Au	$^{196(g+m1+m2)}$Au	^{196m2}Au	$^{195(g+m)}$Au	$^{194(g+m1+m2)}$Au
29.6 ±0.1 (0.2)	1.69 ±0.17	52.1 ±4.2	7.31 ±0.94	84.9 ±6.3	292 ±26
28.8 ±0.1 (0.2)	1.62 ±0.16	63.6 ±5.1	7.36 ±0.92	81.2 ±6.0	330 ±29
28.1 ±0.1 (0.2)	1.74 ±0.17	70.3 ±5.6	7.92 ±0.97	68.7 ±5.1	349 ±30
27.3 ±0.1 (0.2)	1.84 ±0.18	84.4 ±6.8	9.55 ±1.12	66.0 ±4.9	365 ±32
26.5 ±0.1 (0.2)	1.84 ±0.19	90.6 ±7.3	9.00 ±1.05	60.7 ±4.5	379 ±33
25.8 ±0.1 (0.2)	2.05 ±0.20	101 ±8	8.58 ±1.02	61.4 ±4.6	379 ±33
24.9 ±0.1 (0.2)	1.77 ±0.18	94.1 ±7.5	7.83 ±1.06	61.5 ±4.6	348 ±30
24.1 ±0.1 (0.2)	1.71 ±0.18	92.1 ±7.4	6.20 ±0.89	70.8 ±5.3	348 ±30
23.3 ±0.1 (0.2)	1.74 ±0.18	90.6 ±7.2	6.38 ±0.98	92.1 ±6.8	344 ±30
22.4 ±0.1 (0.2)	2.07 ±0.20	88.0 ±7.0	5.85 ±1.08	125 ±9	349 ±30
21.5 ±0.2 (0.2)	2.08 ±0.20	79.8 ±6.4	3.39 ±0.71	163 ±12	361 ±31
20.6 ±0.2 (0.2)	2.10 ±0.20	64.3 ±5.1	2.55 ±0.38	202 ±15	328 ±29
19.6 ±0.2 (0.2)	2.04 ±0.19	49.0 ±3.9	2.08 ±0.34	245 ±18	336 ±29
18.7 ±0.2 (0.2)	2.17 ±0.20	32.1 ±2.6	1.19 ±0.28	273 ±20	355 ±31
17.6 ±0.2 (0.2)	2.19 ±0.20	16.5 ±1.3		254 ±19	347 ±30
16.6 ±0.2 (0.2)	2.16 ±0.20	10.9 ±0.9		245 ±18	366 ±32
15.5 ±0.2 (0.3)	2.21 ±0.20	11.2 ±0.9		209 ±15	307 ±27

14.3 ±0.3 (0.3)	2.45 ±0.22	14.9 ±1.2	181 ±13	269 ±24
13.0 ±0.3 (0.3)	2.96 ±0.25	21.3 ±1.7	147 ±11	221 ±20
11.7 ±0.3 (0.3)	4.05 ±0.33	31.3 ±2.5	108 ±8	156 ±15
10.3 ±0.4 (0.3)	4.30 ±0.35	28.9 ±2.3	56.2 ±4.2	64.3 ±7.6
8.7 ±0.4 (0.4)	2.71 ±0.23	11.7 ±0.9	16.0 ±1.2	15.7 ±3.1
6.9 ±0.5 (0.4)	0.490 ±0.043	1.51 ±0.12	1.87 ±0.18	2.05 ±0.53
4.8 ±0.7 (0.6)	0.0121 ±0.0020	0.0346 ±0.0045		

Table 4.4. Measured cross sections of $^{193, 192, 191}$Au, ^{191}Pt, and $^{192, 190}$Ir in the ^{nat}Pt(p,x) reaction. The projectile energy is listed with total uncertainty and energy loss in parathesis.

E (MeV)	$^{193(g+m)}$Au	$^{192(g+m1+m2)}$Au	$^{191(g+m)}$Au	^{191}Pt(cum)	$^{192(g+m1)}$Ir	$^{190(g+m1+0.086m2)}$Ir
29.6 ±0.1 (0.2)	347 ±55	517 ±72	20.1 ±2.2	19.9 ±3.7	1.40 ±0.12	1.51 ±0.16
28.8 ±0.1 (0.2)	380 ±60	515 ±72	10.3 ±1.6	9.93 ±1.92	1.44 ±0.12	1.43 ±0.15
28.1 ±0.1 (0.2)	367 ±58	466 ±65		4.87 ±1.02	1.34 ±0.11	1.14 ±0.13
27.3 ±0.1 (0.2)	393 ±62	463 ±64		3.72 ±0.82	1.47 ±0.12	1.13 ±0.13
26.5 ±0.1 (0.2)	391 ±62	432 ±60		4.53 ±0.97	1.35 ±0.11	0.897 ±0.116
25.8 ±0.1 (0.2)	391 ±62	420 ±58		4.79 ±1.01	1.29 ±0.11	0.795 ±0.109
24.9 ±0.1 (0.2)	382 ±60	347 ±48	5.70 ±1.43	5.04 ±1.07	1.12 ±0.10	0.497 ±0.091
24.1 ±0.1 (0.2)	383 ±60	298 ±41	6.94 ±1.75	6.48 ±1.32	1.05 ±0.09	0.400 ±0.084
23.3 ±0.1 (0.2)	403 ±63	237 ±33	8.79 ±1.67	8.28 ±1.64	1.05 ±0.09	0.368 ±0.087
22.4 ±0.1 (0.2)	433 ±68	165 ±23	6.86 ±1.64	9.47 ±1.86	1.00 ±0.09	0.227 ±0.068
21.5 ±0.2 (0.2)	446 ±70	81.8 ±11.4	9.25 ±1.65	9.18 ±1.80	0.971 ±0.085	
20.6 ±0.2 (0.2)	415 ±65	21.9 ±3.1	8.18 ±0.92	7.69 ±1.53	0.809 ±0.074	
19.6 ±0.2 (0.2)	351 ±55	2.26 ±0.37	8.15 ±0.90	7.94 ±1.58	0.702 ±0.066	
18.7 ±0.2 (0.2)	291 ±46	0.872 ±0.224	7.20 ±0.85	7.27 ±1.45	0.640 ±0.060	
17.6 ±0.2 (0.2)	256 ±41		7.43 ±0.93	6.40 ±1.30	0.442 ±0.047	
16.6 ±0.2 (0.2)	222 ±35		5.96 ±0.90	5.52 ±1.14	0.326 ±0.038	
15.5 ±0.2 (0.3)	183 ±29		4.88 ±0.89	3.63 ±0.80	0.176 ±0.023	
14.3 ±0.3 (0.3)	141 ±23		3.50 ±0.79	2.79 ±0.65	0.101 ±0.015	
13.0 ±0.3 (0.3)	73.7 ±12.3				0.0409 ±0.0116	
11.7 ±0.3 (0.3)	27.1 ±5.3					

4.3.1 The ^{198g}Au production

The cross sections of the ^{nat}Pt(p,x)^{198g}Au reaction were derived by measuring the gamma line at 411.80205 keV (I_γ = 95.62%) from the decay of ^{198g}Au after a cooling time of 13 days. In addition to

the direct production, ^{198g}Au ($T_{1/2}$ = 2.6941 d) could be formed through the decay of a co-produced metastable state ^{198m}Au ($T_{1/2}$ = 2.272 d, IT: 100%). The possible contribution through ^{198m}Au was negligibly small because intense gamma lines of ^{198m}Au could not be found in the spectra. The cross sections were obtained from the net counts of the photopeak area.

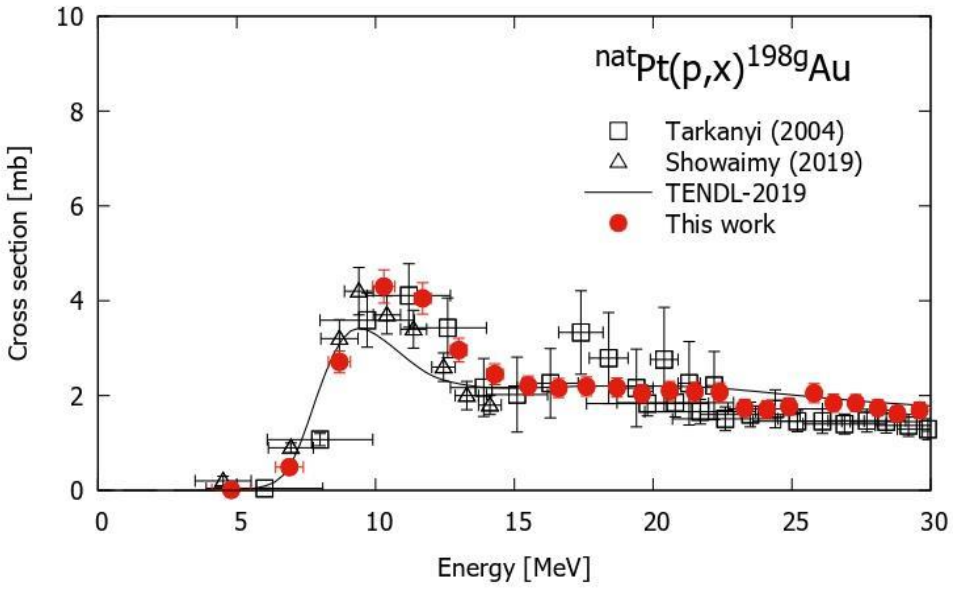

Fig. 4.3. Excitation function of the ^{nat}Pt(p,x)^{198g}Au reaction.

The derived cross sections are shown in Fig. 4.3 and compared with the previous studies (Showaimy et al., 2019; Tárkányi, et al., 2004a) and the TENDL-2019 data (Koning et al., 2019). The literature data normalized to enriched ^{198}Pt targets (Tárkányi et al., 2004a) were re-normalized to natural targets. The present cross-section data show a smooth curve and are consistent with previous experimental data within the uncertainty except for the scattered data of Tárkányi et al. (2004a) at 17-23 MeV. The TENDL-2019 data show the same trend as the experimental excitation function while they slightly underestimate the peak position.

4.3.2 The ^{196g}Au production

The cross sections for ^{196g}Au production were derived by measuring the 355.73-keV gamma line (I_γ = 87%) from the decay of ^{196g}Au ($T_{1/2}$ = 6.1669 d). The measurements of the gamma line were performed after an average cooling time of 13 days. Two metastable states with shorter half-lives ($T_{1/2}$ = 8.1 s and 9.6 h, IT: 100%) decayed to ^{196g}Au during the cooling time. The contributions of the same gamma line from ^{196g}Ir ($T_{1/2}$ = 52 s, β^-: 100%), and ^{196m}Ir ($T_{1/2}$ = 1.4 h, β^-: 100%) could be neglected because of their shorter half-lives.

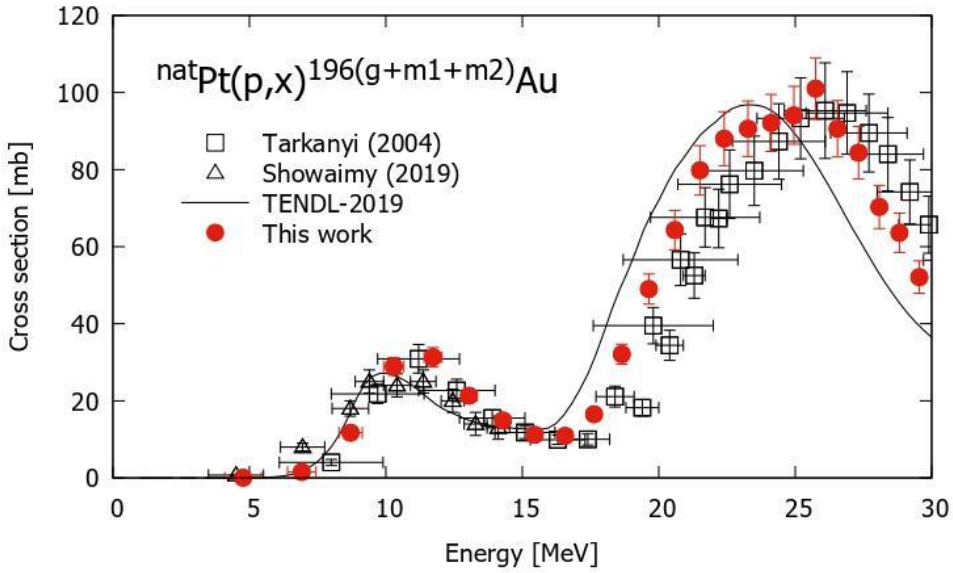

Fig. 4.4. Excitation function of the ^{nat}Pt(p,x)$^{196(g+m1+m2)}$Au reaction.

The cumulative cross sections of $^{196(g+m1+m2)}$Au are shown in Fig. 4.4 together with the previous experimental data (Showaimy et al., 2019; Tárkányi, et al., 2004b) and the TENDL-2019 data (Koning et al., 2019). The data by Tárkányi et al. (2004b) are slightly lower than ours between 17 and 24 MeV while larger above 26 MeV. The experimental data of Showaimy et al. (2019) are in partial agreement with our data. The peak positions of the TENDL-2019 values slightly shifted to the lower energy region although the amplitudes are consistent with the experimental data.

4.3.3 The ^{196m2}Au production

The excitation function of the ^{nat}Pt(p,x)^{196m2}Au reaction was derived from measurements of the gamma line at 147.81 keV (I_γ = 43.5%) from the ^{196m2}Au decay ($T_{1/2}$ = 9.6 h). The measurements were performed after a cooling time of 21 hours. The interference of the 147.49-keV gamma line (I_γ = 0.77%) from ^{191}Au ($T_{1/2}$ = 3.18 h) was negligibly small because the more intense gamma line at 586.44 keV (I_γ = 15.0%) of ^{191}Au disappeared in the used spectra.

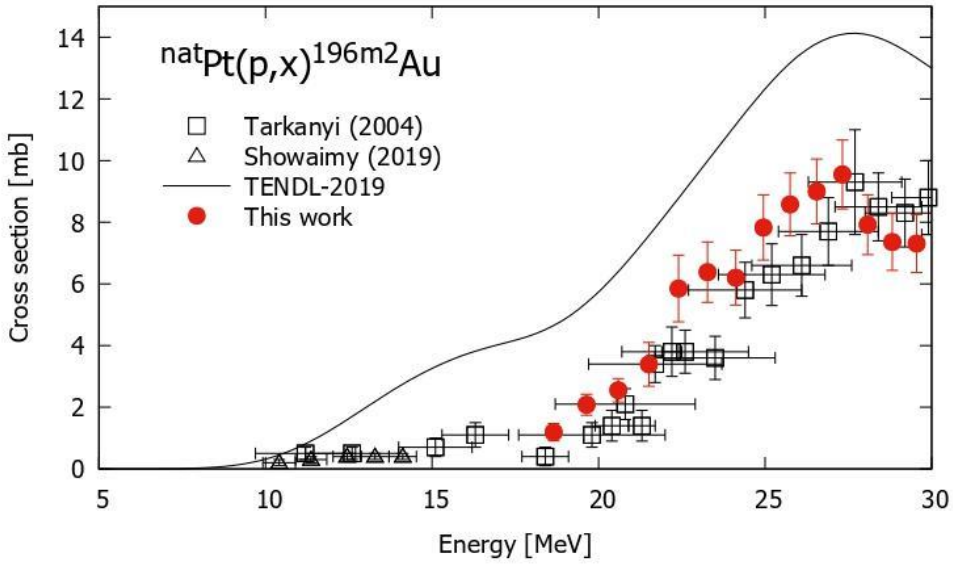

Fig. 4.5. Excitation function of the ^{nat}Pt(p,x)^{196m2}Au reaction.

The cross sections are shown in Fig. 4.5 together with the previous experimental data (Showaimy et al., 2019; Tárkányi, et al., 2004b) and the TENDL-2019 data (Koning et al., 2019). Our result measured in the energy range between 19 and 30 MeV is consistent with the data of Tárkányi et al. (2004b) within the uncertainty. The data of Showaimy et al. (2019) are not overlapped with ours but are consistent with the other experimental result. The TENDL-2019 data overestimate the experimental cross sections.

4.3.4 The ^{195g}Au production

The cross sections for the ^{195g}Au production were derived using spectra measured after an average cooling time of 69 days. The metastable state ^{195m}Au with a short half-life ($T_{1/2}$ = 30.5 s, IT: 100%) decayed to the ground state ^{195g}Au ($T_{1/2}$ = 186.01 d) soon after the end-of-bombardment. The 98.857-keV gamma line (I_γ = 11.21%) from the decay of ^{195g}Au was used to derive the cross sections. The possible contribution to the same gamma line from ^{195m}Pt ($T_{1/2}$ = 4.01 d, IT: 100%) was negligible after the long cooling time. The self-absorption of the low-energy gamma line was calculated using equation (4.1) and the correction factor was estimated as 1.11. The measured activities were corrected by multiplying the factor.

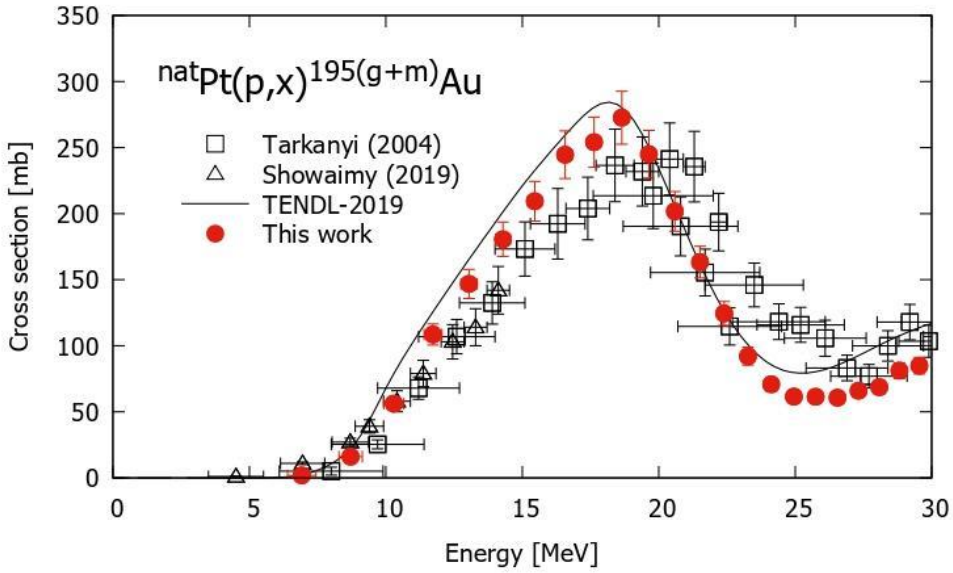

Fig. 4.6. Excitation function of the $^{nat}Pt(p,x)^{195(g+m)}Au$ reaction.

The cumulative cross sections of $^{195(g+m)}Au$ using the corrected activities are shown in Fig. 4.6 together with the previous experimental data (Showaimy et al., 2019; Tárkányi et al., 2004b) and the TENDL-2019 data (Koning et al., 2019). Both previous experimental data of Showaimy et al. (2019) and Tárkányi et al. (2004b) are in partial agreement with our data. The TENDL-2019 values show a trend and amplitude similar to the experimental excitation functions while its peak energy seems slightly higher.

4.3.5 The ^{194g}Au production

The cross sections of the $^{nat}Pt(p,x)^{194g}Au$ reaction were derived using spectra measured after a cooling time of 21 hours. Two co-produced short-lived metastable states ($T_{1/2}$ = 600 and 420 ms, IT: 100%) decayed to the ground state ^{194g}Au ($T_{1/2}$ = 38.02 h) soon after the irradiation. Intense gamma lines at 328.47 keV (I_γ = 62.8%) and 293.549 keV (I_γ = 10.9%) from the decay of ^{194g}Au were interfered with those from decays of the ground state ($T_{1/2}$ = 19.28 h) and an excited state of ^{194}Ir ($T_{1/2}$ = 171 d). The interference-free gamma line at 1468.904 keV (I_γ = 6.8%) was instead selected. The gamma line also included the contribution from ^{194g}Ir (I_γ = 0.186%), which was confirmed to be negligible based on decay curve analysis. The cumulative cross sections were obtained from the net counts of the photopeak area.

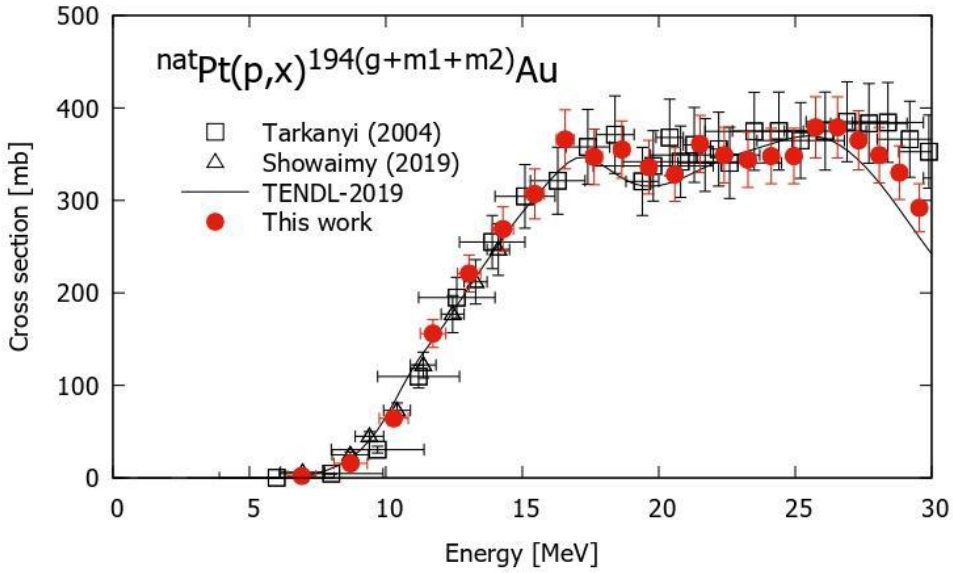

Fig. 4.7. Excitation function of the ^{nat}Pt(p,x)$^{194(g+m1+m2)}$Au reaction.

The cumulative cross sections of $^{194(g+m1+m2)}$Au are shown in Fig. 4.7 and compared with the previous studies (Showaimy et al., 2019; Tárkányi et al., 2004b) and the TENDL-2019 data (Koning et al., 2019). Our result is in good agreement with both previous experimental data below 16 MeV. The data of Tárkányi et al. (2004b) are slightly larger than ours above 27 MeV. The TENDL-2019 values agree well with the experimental data.

4.3.6 The ^{193g}Au production

Measurements of the 255.57-keV gamma line (I_γ = 6.5%) after a cooling time longer than 21 hours were used to derive the production cross sections of ^{193g}Au ($T_{1/2}$ = 17.65 h). The metastable state ^{193m}Au ($T_{1/2}$ = 3.9 s, IT: 99.97%) decayed during the irradiation. The more intense gamma line at 186.17 keV (I_γ = 9.7%) was unselected to avoid the interference of the 186.68-keV gamma line from the ground state ($T_{1/2}$ = 11.78 d, I_γ = 50%), and an excited state of ^{190}Ir ($T_{1/2}$ = 3.087 h, I_γ = 64.37%).

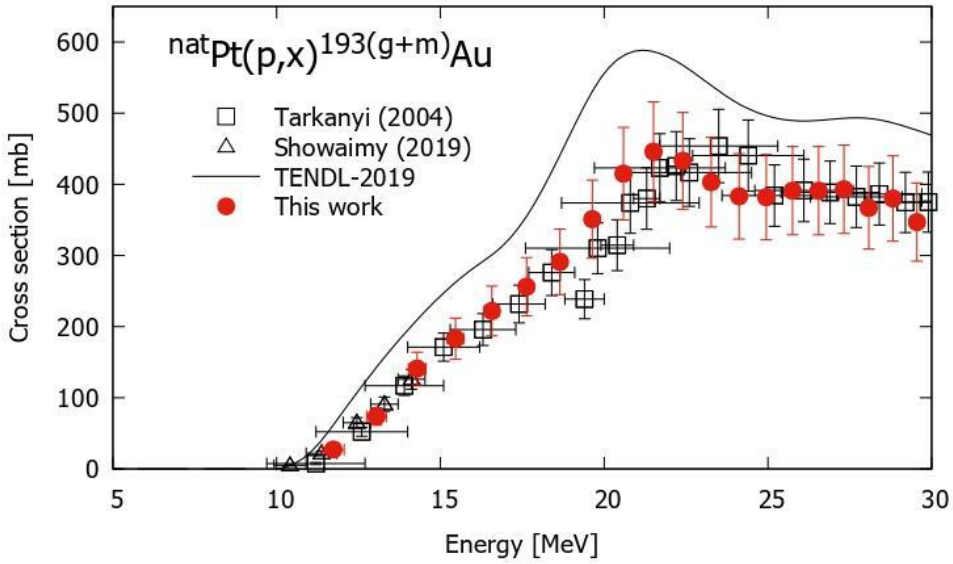

Fig. 4.8. Excitation function of the $^{nat}Pt(p,x)^{193(g+m)}Au$ reaction.

The cumulative cross sections of $^{193(g+m)}Au$ are shown in Fig. 4.8 in comparison with the previous experimental data (Showaimy et al., 2019; Tárkányi et al., 2004b) and the TENDL-2019 data (Koning et al., 2019). The present data are in good agreement with the previous data of Showaimy et al. (2019) and Tárkányi et al. (2004b). The TENDL-2019 data overestimate the experimental cross sections.

4.3.7 The ^{192g}Au production

The cross sections of the $^{nat}Pt(p,x)^{192g}Au$ reaction were derived from the measurements of the 316.50618-keV gamma line (I_γ = 59%) emitted with the ^{192g}Au decay ($T_{1/2}$ = 4.94 h) after cooling time of 2 hours. Two metastable states ($T_{1/2}$ = 29 and 160 ms, IT: 100%) decayed during the irradiation. The contribution to the same gamma line (I_γ = 82.86%) from ^{192g}Ir ($T_{1/2}$ = 73.829 d) was neglected because of the long half-life and small cross sections (see section 4.3.10). The contribution of the gamma line at 316.19 keV (I_γ = 3.0%) from $^{196m2}Au$ ($T_{1/2}$ = 9.6 h) was estimated using another intense gamma line at 147.81 keV (I_γ = 43.5%) and found to be negligibly small.

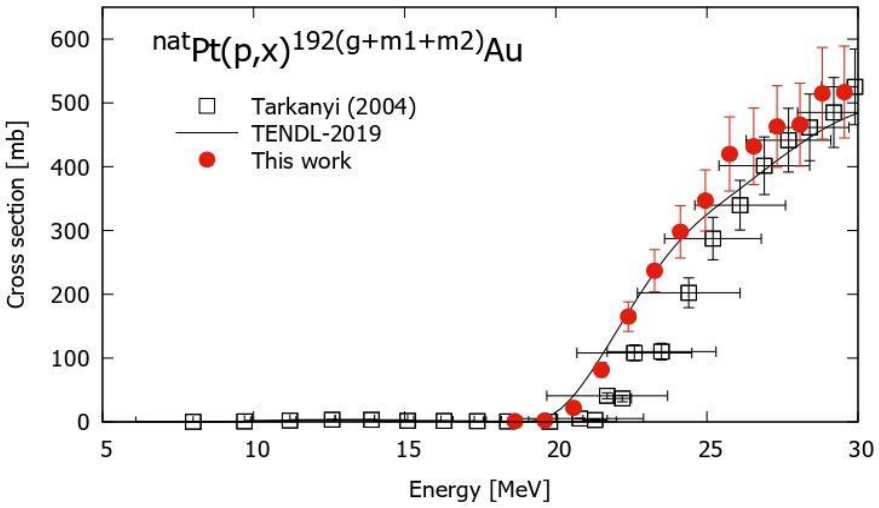

Fig. 4.9. Excitation function of the ^{nat}Pt(p,x)$^{192(g+m1+m2)}$Au reaction.

The cumulative cross sections of $^{192(g+m1+m2)}$Au are shown in Fig. 4.9 in comparison with the previous experimental data (Tárkányi et al., 2004b) and the TENDL-2019 data (Koning et al., 2019). The data reported by Tárkányi et al. (2004b) are consistent with ours except for a few data at 22-24 MeV. The TENDL-2019 data are roughly consistent with experimental results.

4.3.8 The ^{191g}Au production

Measurements of the 586.44-keV gamma line (I_γ = 15%) after a cooling time of 2 hours were used to derive the production cross sections of ^{191g}Au ($T_{1/2}$ = 3.18 h). The metastable state ^{191m}Au ($T_{1/2}$ = 0.92 s, IT: 100%) decayed to the ground state during the irradiation.

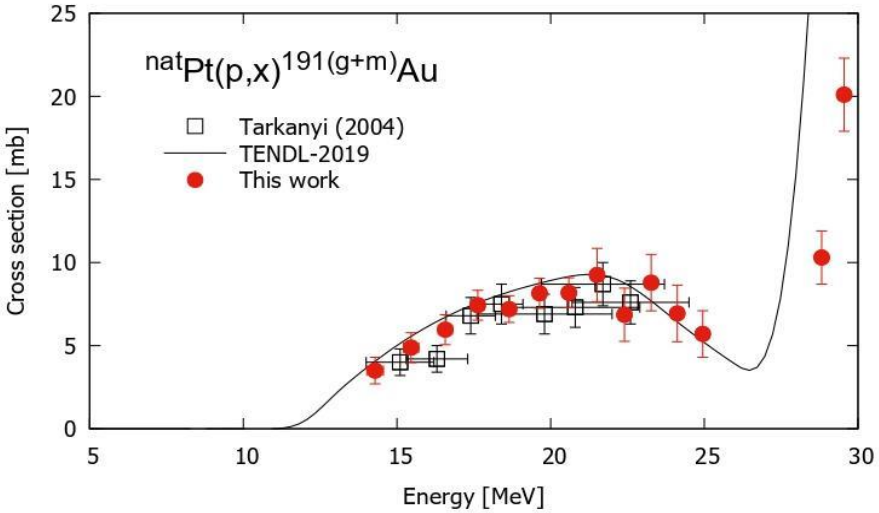

Fig. 4.10. Excitation function of the ^{nat}Pt(p,x)$^{191(g+m)}$Au reaction.

The cumulative cross sections of $^{191(g+m)}$Au are shown in Fig. 4.10 in comparison with the previous experimental data (Tárkányi et al., 2004b) and the TENDL-2019 data (Koning et al., 2019). Our result is consistent with the data of Tárkányi et al. (2004b) within uncertainty. The TENDL-2019 data are larger than experimental data above 29 MeV.

4.3.9 The ^{191}Pt production

The production cross sections of ^{191}Pt ($T_{1/2}$ = 2.83 d) were derived from the gamma line at 538.87 keV (I_γ = 14.3%). We used the gamma spectra recorded after a cooling time of 13 days. Its parent radionuclide ^{191}Au ($T_{1/2}$ = 3.18 h) decayed to ^{191}Pt completely during the cooling time. The derived cumulative cross sections of ^{191}Pt were, however, smaller than the independent cross sections of ^{191}Au. This inconsistency was caused by large uncertainties of gamma-ray intensities (12% for ^{191}Au and 17% for ^{191}Pt) and net-count statistics (4-30%).

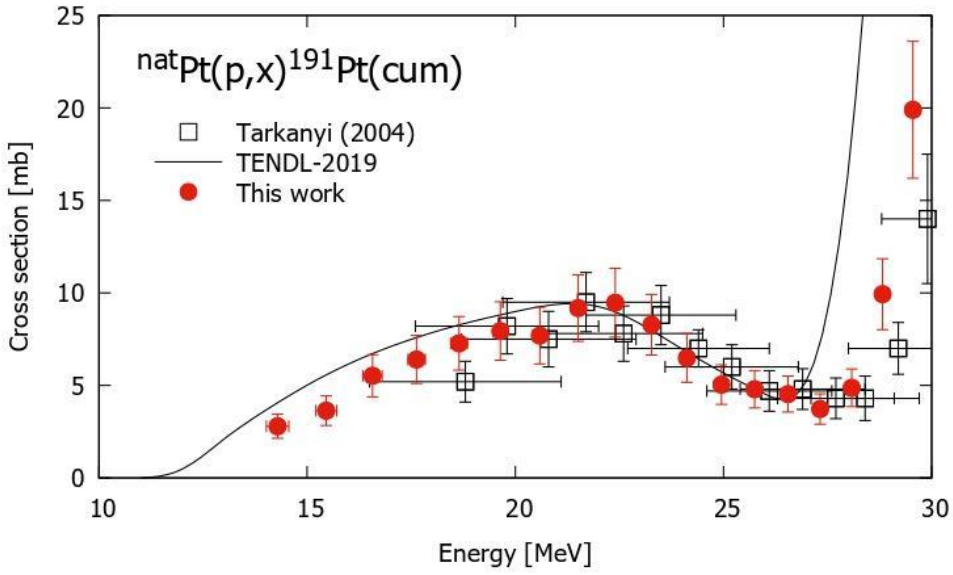

Fig. 4.11. Excitation function of the ^{nat}Pt(p,x)^{191}Pt(cum) reaction.

The cumulative cross sections are shown in Fig. 4.11 together with the previous experimental data (Tárkányi et al., 2004b) and the TENDL-2019 data (Koning et al., 2019). The present data are consistent with the data of Tárkányi et al. (2004b) within uncertainty. The TENDL-2019 data are roughly consistent with experimental results and overestimate above 26 MeV.

4.3.10 The ^{192g}Ir production

The cross sections of the ^{nat}Pt(p,x)^{192g}Ir reaction were derived from the measurements of the 316.50618-keV gamma line (I_γ = 82.86%) emitted with the ^{192g}Ir decay ($T_{1/2}$ = 73.829 d) after an

average cooling time of 69 days. The short-lived metastable state ^{192m}Ir ($T_{1/2}$ = 1.45 m, IT: 99.98%) decayed to ^{192g}Ir soon after the end-of-bombardment. The second metastable state has a very long half-life ($T_{1/2}$ = 241 y, IT: 100%) and its decay less contributed to spectra. The contribution of ^{192g}Au ($T_{1/2}$ = 4.94 h) to the same gamma line was negligible because it completely decayed during the cooling time.

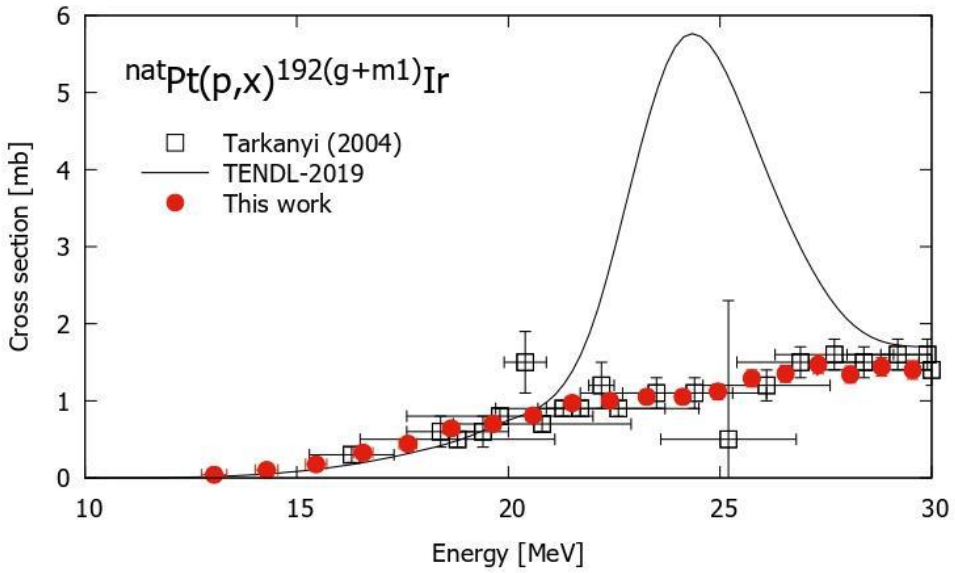

Fig. 4.12. Excitation function of the ^{nat}Pt(p,x)$^{192(g+m1)}$Ir reaction.

The cumulative cross sections of $^{192(g+m1)}$Ir are shown in Fig. 4.12 in comparison with the previous experimental data (Tárkányi et al., 2004b) and the TENDL-2019 data (Koning et al., 2019). The present cross-section data show a smooth curve and are consistent with the data reported by Tárkányi et al. (2004b). The TENDL-2019 values have a different shape from the experimental ones in the 21-29 MeV energy region.

4.3.11 The ^{190g}Ir production

The cross sections for ^{190g}Ir production were derived by measuring the 186.68-keV gamma line (I_γ = 50%) from the decay ($T_{1/2}$ = 11.78 d). The measurements were performed after an average cooling time of 13 days. Two metastable states with shorter half-lives ($T_{1/2}$ = 1.12 h, IT: 100% and $T_{1/2}$ =3.087 h, IT: 8.6%) decayed to ^{190g}Ir or ^{190}Os during the cooling time. The interference of the gamma lines at 186.17 keV (I_γ = 9.7%) from ^{193g}Au ($T_{1/2}$ = 17.65 h) and 188.27 keV (I_γ = 30.0%) from ^{196m2}Au ($T_{1/2}$ = 9.6 h) was negligible after the long cooling time.

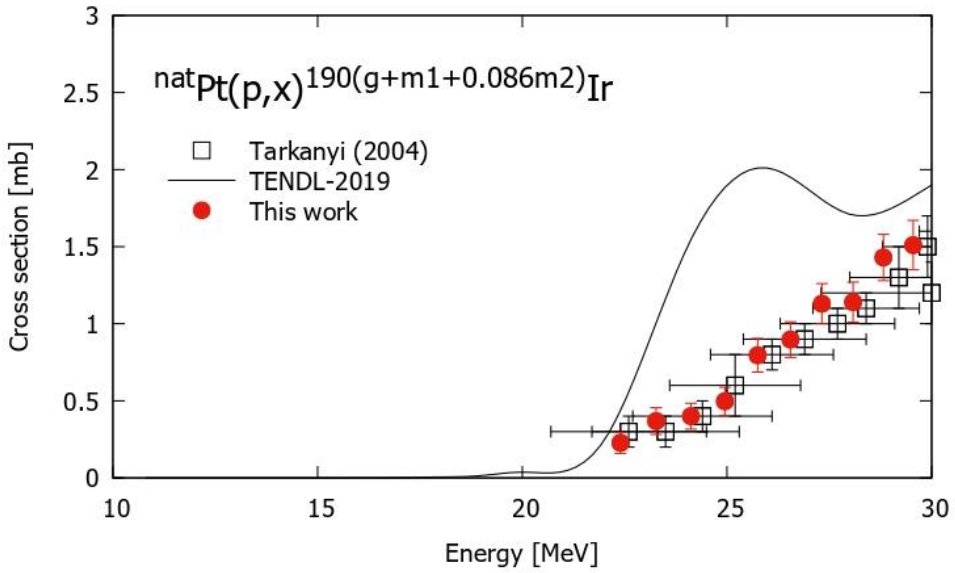

Fig. 4.13. Excitation function of the $^{nat}Pt(p,x)^{190(g+m1+0.086m2)}Ir$ reaction.

The cumulative cross sections of $^{190(g+m1+0.086m2)}Ir$ are shown in Fig. 4.13 together with the previous experimental data (Tárkányi et al., 2004b) and the TENDL-2019 data (Koning et al., 2019). The previous data are in good agreement with ours. The TENDL-2019 values overestimate the experimental data and show a different shape.

4.4 Summary

Activation cross sections of the proton-induced reactions on ^{nat}Pt were measured up to 30 MeV at the RIKEN AVF cyclotron. The stacked-foil activation technique and the high-resolution gamma-ray spectrometry were used for the cross-section measurements. The excitation functions for 11 radioisotopes $^{198, 196, 196m2, 195, 194, 193, 192, 191}$Au, ^{191}Pt, and $^{192, 190}$Ir were determined and compared with data published earlier and the TENDL-2019 library.

Our measured excitation functions show smooth curves and are in acceptable agreement with the previous studies of Showaimy et al. (2019) and Tárkányi et al. (2004a, 2004b) within uncertainty. Our results can contribute to nuclear reaction databases required for the optimization of the ^{198}Au production.

CHAPTER 5: CONCLUSION

We studied the production cross sections (excitation functions) of medical radioisotopes ^{52g}Mn and ^{198g}Au via charged-particle-induced reactions. Two experiments were performed at the AVF cyclotron of the RIKEN RI Beam Factory. We adopted well-established methods of stacked-foil activation technique and gamma-ray spectrometry to determine activation cross sections. The measured data are compared with previous experimental data and the theoretical calculations in the TENDL-2019 library.

In the first experiment, we measured the excitation functions of the alpha-particle-induced reactions on ^{nat}V up to 50 MeV. The production cross sections of ^{52g}Mn and co-produced ^{54}Mn, ^{51}Cr, ^{48}V, and $^{47, 46g}$Sc were determined. The derived excitation function of the ^{nat}V(α,x)^{52g}Mn reaction is compared with the literature data and TENDL-2019 values. Among the eleven previous studies, only the data by Levkovski (1991) are consistent with our result. The physical yield of ^{52g}Mn was deduced from the measured cross sections and found to be larger than the experimental data of Dmitriev et al. (1969).

In the second experiment, activation cross sections of the proton-induced reactions on ^{nat}Pt were measured up to 30 MeV. The excitation functions for production of eleven radioisotopes $^{198, 196, 196m2, 195, 194, 193, 192, 191}$Au, ^{191}Pt, and $^{192, 190}$Ir were determined. Our measured excitation functions show smooth curves. The previous studies are in acceptable agreement with ours within uncertainty. The TENDL-2019 values are slightly different from our result.

Our measured cross sections are less scattered and more reliable than most of the literature data. The reliable cross sections can enhance and improve nuclear reaction databases. The results can also contribute to the optimization of the production of ^{52g}Mn and ^{198g}Au for medical use and the development of theoretical model calculation codes.

The production cross sections of medical radioisotopes and optimization of their production routes will be studied continuously in the future. In addition, we will expand the scope of the research under collaboration with researchers in the other fields, e.g., chemistry and nanoparticles. With knowledge of chemistry, targets other than metallic foils can be prepared and chemical separation for practical use can be examined. Collaborative research with nanoparticle researchers can study radioactive nanoparticles for a variety of applications.

Appendix

A. Target thickness

The target thickness n [mg/cm^2] was derived using the measured size and weight of the foil by a caliper and electronic balance (Fig. A.1). The weight and size were measured several times and the average values were derived. The thickness of the foils was derived using equation (A.1) as follows:

$$n_T = \frac{m}{S} \tag{A.1}$$

where m [g] and S [cm^2] were the measured weight and size of the foil, respectively.

Fig. A.1. (a) Caliper and, (b) electronic balance

B. HPGe detector

The gamma-ray spectra of irradiated foils were measured without chemical separation using a high-resolution HPGe detector (ORTEC GEM-25185-P). The detector has a p-type point contact and is designed for high-resolution gamma-ray spectroscopy. The crystal size of GEM-25185-P is about 2"×2"×1" and the detector has a high resolution of about 1.8 keV at 1.33 MeV. The detector is efficient at detecting gamma rays with an efficiency of about 70% at 1 MeV and 40% at 2 MeV. The gamma-ray spectra were analyzed by the dedicated software (SEIKO EG&G Gamma Studio) as shown in Fig. A. 2.

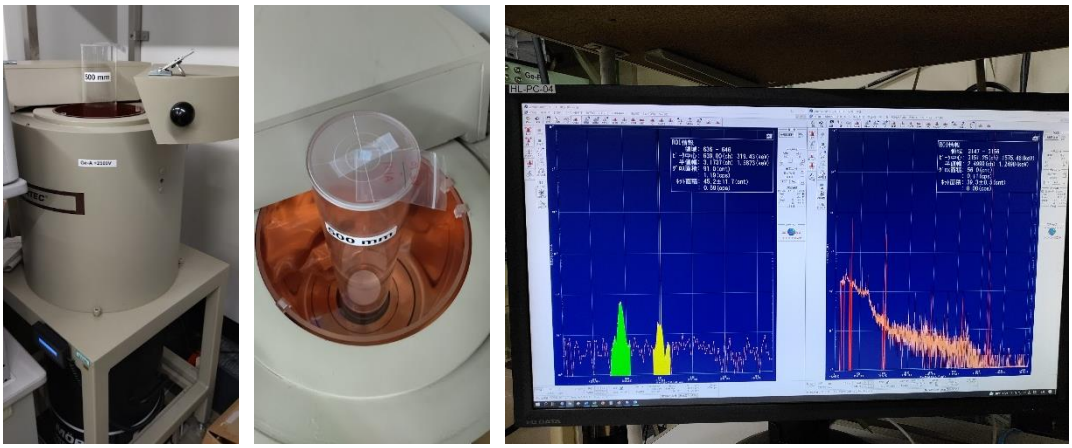

Fig. A.2. Gamma spectrometry system with high-resolution HPGe detector (ORTEC GEM-25185-P) at RIKEN

C. Detector efficiency

Gamma rays emitted from the foils were detected with a certain probability due to a variety of factors, such as attenuation, Compton scattering, and absorption. These factors affect the detection probability of gamma rays. The probability of detecting a gamma ray is often referred to as the detector efficiency (ε_d). It is defined as the ratio of the number of detected gamma rays to the number of gamma rays incoming to the detector. The detector efficiency can be determined by a calibration source with known activity. By measuring the activity of the calibration source with the detector and comparing it to the known activity, the detector efficiency can be calculated.

In our experiments, a multiple gamma-ray emitting point source consisting of radionuclides, ^{57,60}Co, ^{85}Sr, ^{88}Y, ^{109}Cd, ^{113}Sn, ^{137}Cs, ^{139}Ce, ^{203}Hg, and ^{241}Am (Eckert & Ziegler Isotope Products), was used to calibrate the detector.

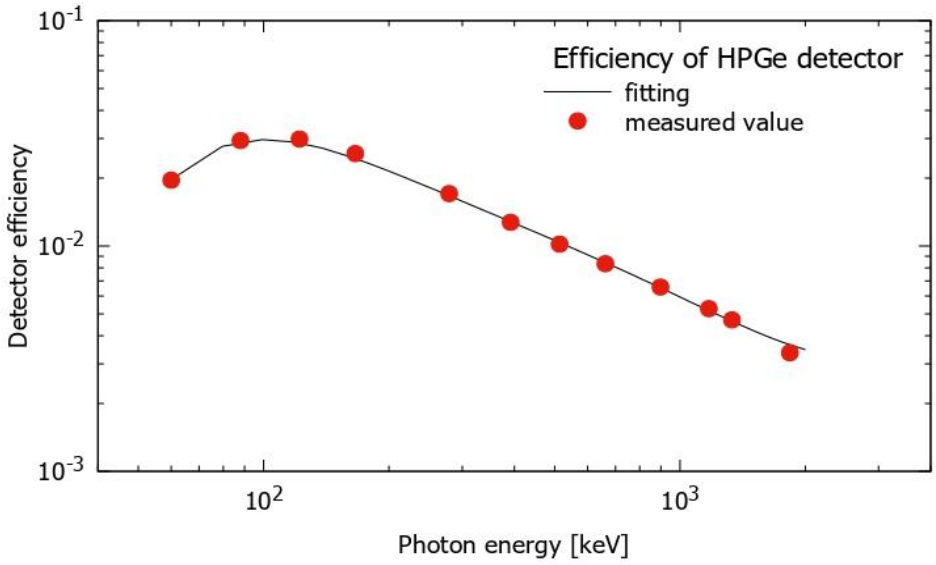

Fig. A.3. An example of efficiency calibration for an HPGe detector at 5 cm using a multiple gamma-ray point source

D. Calibration source

The detector was calibrated by a multiple gamma-ray emitting point source (Eckert & Ziegler Isotope Products) consisting of radioisotopes listed in Table A.1.

Table A.1. Calibration sources and their data by the HPGe detector

Energy (keV)	Radionuclide	Half-life		Branch ratio (%)
60	Am-241	432.17	y	36
88	Cd-109	462.6	d	3.63
122	Co-57	271.79	d	85.6
166	Ce-139	137.64	d	79.9
279	Hg-203	46.595	d	81.5
392	Sn-133	115.09	d	64.9
514	Sr-85	64.849	d	98.4
662	Cs-137	30.17	y	85.1
898	Y-88	106.63	d	94
1173	Co-60	5.272	y	99.86
1333	Co-60	5.272	y	99.98
1836	Y-88	106.63	d	99.4

Acknowledgments

I express profound gratitude for the M-JEED (Mongolian-Japan Engineering Education Development Program) scholarship that opened doors for my doctoral studies and research at the Graduate School of Biomedical Science and Engineering, Hokkaido University. The support has allowed me to make meaningful progress in my academic pursuit, and I'm forever thankful.

I extend heartfelt thanks to all who supported and guided me during my research journey. Their steadfast help, mentorship, and aid were crucial to the success of my work. I'm grateful for the time, expertise, and resources they graciously shared and for their impact on shaping my research.

I'm immensely grateful to my supervisor, Prof. Masayuki Aikawa, support and guidance throughout my research. His wisdom and encouragement were priceless. I also thank my colleagues at the Medical Applied Basic Physics Laboratory at the Graduate School of Biomedical Science and Engineering, Hokkaido University, who made the research process a collaborative and enjoyable experience with their cooperation.

I express sincere appreciation to Prof. Erdene Norov, Prof. Tegshjargal Khishigjargal, and colleagues at the Department of Chemical and Biological Engineering, National University of Mongolia. Their exceptional leadership, broad vision, belief, and positivity provided me with steadfast support and encouragement during difficult times in my research. I'm thankful for their guidance, support, and crucial impact on my academic journey.

I thank the members of the RI Application Research Group at RIKEN Nishina Center for their teamwork in conducting experiments. I sincerely thank a group leader, Dr. Hiromitsu Haba, for his support, encouragement, and provision of excellent experimental conditions. His mentorship and aid have significantly shaped my research, and I'm deeply grateful for his positive impact on my work.

I'm grateful to Prof. Zuzaan Purev and Prof. Otgooloi Banzarjav, my former supervisors, for their invaluable guidance and long-term support during my research journey. I'm also thankful to my colleagues at the Nuclear Research Center of the National University of Mongolia for their collaboration and support. Their expertise and encouragement have been instrumental in shaping my work, and I'm deeply thankful for their positive impact on my academic journey.

I'm forever grateful to my parents, Gantumur Sovd and Oyuntsetseg Molomjav, for their boundless love and support throughout my life. I also thank my family, especially my wife, Tsembelmaa Gereltsaikhan, for her constant encouragement and support, and my children for bringing happiness to my life. I extend my gratitude to my brothers and sisters and their families for their unwavering support and inspiration. Their love and support have been the foundation of my success, and I'm deeply thankful for their role in my life.

I'm grateful to those who have allowed me to conduct research. I want to express my gratitude to the RI Beam Factory, operated by RIKEN Nishina Center and CNS, University of Tokyo, Japan, for providing the facilities for carrying out the experiments.

Finally, I'm thankful for the M-JEED scholarship (Mongolian-Japan Engineering Education Development Program, J11B16) support, which allowed me to achieve my academic aspirations. I extend gratitude to JSPS KAKENHI Grant No. 22H04961 for their financial support, which significantly impacted my research. Their backing was essential in making my research successful, and I'm deeply thankful for their kindness.

Cited References

Alauddin, M. M. (2012). Positron emission tomography (PET) imaging with (18)F-based radiotracers. American Journal of Nuclear Medicine and Molecular Imaging, 2, 55-76.

Alfassi, Z. B., Persico, E., Groppi, F., & Bonardi, M. L. (2009). On the photon self-absorption correction for thin-target-yields vs. thick-target-yields in radionuclide production. Applied Radiation and Isotopes, 67, 240-242. https://doi.org/10.1016/j.apradiso.2008.10.004

Ali, B. M., Al-Abyad, M., Seddik, U., El-Kameesy, S. U., Ditrói, F., Takács, S., & Tárkányi, F. (2018). Activation cross-section data for α-particle-induced nuclear reactions on natural vanadium for practical applications. Pramana - Journal of Physics 90, 41. https://doi.org/10.1007/s12043-018-1527-z

Baum, R. P., & Kulkarni, H. R. (2012). Theranostics: From molecular imaging using Ga-68 labeled tracers and PET/CT to personalized radionuclide therapy - the bad berka experience. In Theranostics, 2, 437-447. https://doi.org/10.7150/thno.3645

Benešová, M., & Reischl, G. (2022). Production of radionuclides: Cyclotrons and reactors. Nuclear Medicine and Molecular Imaging, 1, 52–65. https://doi.org/10.1016/B978-0-12-822960-6.00003-X

Bianchi, F., Marchi, C., Fuad, G., Groppi, F., Haddad, F., Magagnin, L., & Manenti, S. (2020). On the production of ^{52g}Mn by deuteron irradiation on natural chromium and its radionuclidic purity. Applied Radiation and Isotopes, 166, 109329. https://doi.org/10.1016/j.apradiso.2020.109329

Bindu, K. B., Mukheijee, S., & Singh, N. L. (1998). Pre-equilibrium model analysis of alpha particle induced reactions up to 80 MeV. Physica Scripta, 57, 201-206. https://doi.org/10.1088/0031-8949/57/2/007

Black, K. C. L., Wang, Y., Luehmann, H. P., Cai, X., Xing, W., Pang, B., Zhao, Y., Cutler, C. S., Wang, L. V., Liu, Y., & Xia, Y. (2014). Radioactive ^{198}Au-doped nanostructures with different shapes for in vivo analyses of their biodistribution, tumor uptake, and intratumoral distribution. ACS Nano, 8, 4385–4394. https://doi.org/10.1021/nn406258m

Boros, E., Marquez, B. v., Ikotun, O. F., Lapi, S. E., & Ferreira, C. L. (2014). Coordination Chemistry and Ligand Design in the Development of Metal Based Radiopharmaceuticals. In Ligand Design in Medicinal Inorganic Chemistry. https://doi.org/10.1002/9781118697191.ch3

Boros, E., & Packard, A. B. (2019). Radioactive Transition Metals for Imaging and Therapy. In Chemical Reviews, 119, 870–901. https://doi.org/10.1021/acs.chemrev.8b00281

Bowman, W. W., & Blann, M. (1969). Reactions of ^{51}V and ^{27}Al with 7-120 MeV α-particles (equilibrium and non-equilibrium statistical analyses). Nuclear Physics, Section A, 131, 513-531. https://doi.org/10.1016/0375-9474(69)90592-2

Buchegger, F., Perillo-Adamer, F., Dupertuis, Y. M., & Bischof Delaloye, A. (2006). Auger radiation targeted into DNA: A therapy perspective. In European Journal of Nuclear Medicine and Molecular Imaging, 33, 1352–1363. https://doi.org/10.1007/s00259-006-0187-2

Chakravarty, R., Chakraborty, S., Guleria, A., Kumar, C., Kunwar, A., Nair, K. V. V., Sarma, H. D., & Dash, A. (2019). Clinical scale synthesis of intrinsically radiolabeled and cyclic RGD peptide functionalized ^{198}Au nanoparticles for targeted cancer therapy. Nuclear Medicine and Biology, 72, 1-10. https://doi.org/10.1016/j.nucmedbio.2019.05.005

Chanda, N., Kan, P., Watkinson, L. D., Shukla, R., Zambre, A., Carmack, T. L., Engelbrecht, H., Lever, J. R., Katti, K., Fent, G. M., Casteel, S. W., Smith, C. J., Miller, W. H., Jurisson, S., Boote, E., Robertson, J. D., Cutler, C., Dobrovolskaia, M., Kannan, R., & Katti, K. v. (2010). Radioactive gold nanoparticles in cancer therapy: therapeutic efficacy studies of GA-^{198}AuNP nanoconstruct in prostate tumor-bearing mice. Nanomedicine: Nanotechnology, Biology, and Medicine, 6, 201-209. https://doi.org/10.1016/j.nano.2009.11.001

Chowdhury, D. P., Pal, S., Saha, S. K., & Gangadharan, S. (1995). Determination of cross section of α-induced nuclear reaction on natural Cr and Zr by stacked foil activation for thin layer activation analysis. Nuclear Inst. and Methods in Physics Research, B, 103, 261-266. https://doi.org/10.1016/0168-583X(95)00663-X

Chu, S. Y. F., Ekström, L. P., & Firestone, R. B. (1999). The LUND/LBNL nuclear data search (version 2.0) [WWW Document]. URL http://nucleardata.nuclear.lu.se/toi/

Dmitriev, P. P., Konstantinov, I. O., & Krasnov, N. N. (1969). Methods for producing the ^{52}Mn isotope. In Soviet Atomic Energy, 26, 539–541. https://doi.org/10.1007/BF01174115

Engle, J. W., Ignatyuk, A. v., Capote, R., Carlson, B. v., Hermanne, A., Kellett, M. A., Kibédi, T., Kim, G., Kondev, F. G., Hussain, M., Lebeda, O., Luca, A., Nagai, Y., Naik, H., Nichols, A. L., Nortier, F. M., Suryanarayana, S. v., Takács, S., Tárkányi, F. T., & Verpelli, M. (2019). Recommended Nuclear Data for the Production of Selected Therapeutic Radionuclides. Nuclear Data Sheets, 155, 56–74. https://doi.org/10.1016/J.NDS.2019.01.003

Fernandes, M. A. R., Andrade, A. L. de, Biazzono, L., Luvizotto, M. C. R., Santos, A. dos, & Correa, C. (2003). Gold (^{198}Au) foils brachytherapy use on canine skin tumor. Brazilian Journal of Veterinary Research and Animal Science, 40, 321-327. https://doi.org/10.1590/s1413-95962003000500002

Hansper, V. Y., Morton, A. J., Tims, S. G., Tingwell, C. I. W., Scott, A. F., & Sargood, D. G. (1993). Cross sections and thermonuclear reaction rates for $^{51}V(\alpha, n)^{54}Mn$ and $^{51}V(\alpha, p)^{54}Cr$. Nuclear Physics, Section A, 551, 158-172. https://doi.org/10.1016/0375-9474(93)90309-L

Hermanne, A., Ignatyuk, A. v., Capote, R., Carlson, B. v., Engle, J. W., Kellett, M. A., Kibédi, T., Kim, G., Kondev, F. G., Hussain, M., Lebeda, O., Luca, A., Nagai, Y., Naik, H., Nichols, A. L., Nortier, F. M., Suryanarayana, S. V., Takács, S., Tárkányi, F. T., & Verpelli, M. (2018). Reference Cross Sections for Charged-particle Monitor Reactions. Nuclear Data Sheets, 148, 338-382. https://doi.org/10.1016/j.nds.2018.02.009

Horiuchi, J., Takeda, M., Shibuya, H., Matsumoto, S., Hoshina, M., & Suzuki, S. (1991). Usefulness of ^{198}Au grain implants in the treatment of oral and oropharyngeal cancer. Radiotherapy and Oncology, 21, 29-38. https://doi.org/10.1016/0167-8140(91)90338-H

Hubbel, J. H., & Seltzer, S. M. (2004). Tables of X-Ray Mass Attenuation Coefficients and Mass Energy-Absorption Coefficients (version 1.4). [Online] National Institute of Standards and Technology, Gaithersburg, MD. https://dx.doi.org/10.18434/T4D01F

Iguchi, A., Amano, H., & Tanaka, S. (1960). (α, n) Cross Sections for ^{48}Ti and ^{51}V. Journal of the Atomic Energy Society of Japan / Atomic Energy Society of Japan, 2, 682-684. https://doi.org/10.3327/jaesj.2.682

International Atomic Energy Agency. (2003). Manual for Reactor Produced Radioisotopes (IAEA-TECDOC-1340) [Online]. URL https://www.iaea.org/publications/6407/manual-for-reactor-produced-radioisotopes

International Atomic Energy Agency. (2009a). Cyclotron Produced Radionuclides: Principles and Practice (IAEA, Technical Reports Series No. 465) [Online]. URL https://www.iaea.org/publications/7849/cyclotron-produced-radionuclides-principles-and-practice

International Atomic Energy Agency. (2009b). LiveChart of Nuclides [WWW Document]. URL https://www-nds.iaea.org/livechart/

International Atomic Energy Agency. (2023). IAEA - Medical portal [WWW Document]. URL https://www-nds.iaea.org/relnsd/vcharthtml/MEDVChart.html

Ismail, M. (1993). Measurement of excitation functions and mean projected recoil ranges of nuclei in α-induced reactions on F, Al, V, Co and Re nuclei. Pramana, 40, 227-251. https://doi.org/10.1007/BF02900190

Karvat, A., Duzenli, C., Ma, R., Paton, K., & Pickles, T. (2001). The treatment of choroidal melanoma with ^{198}Au plaque brachytherapy. Radiotherapy and Oncology, 59, 153-156. https://doi.org/10.1016/S0167-8140(00)00334-0

Kassis, A. I. (2008). Therapeutic Radionuclides: Biophysical and Radiobiologic Principles. Seminars in Nuclear Medicine, 38, 358–366. https://doi.org/10.1053/J.SEMNUCLMED.2008.05.002

Koning, A. J., Rochman, D., Sublet, J. C., Dzysiuk, N., Fleming, M., & van der Marck, S. (2019). TENDL: Complete Nuclear Data Library for Innovative Nuclear Science and Technology. Nuclear Data Sheets, 155, 1-55. https://doi.org/10.1016/j.nds.2019.01.002

Konishi, M., Fujita, M., Takeuchi, Y., Kubo, K., Imano, N., Nishibuchi, I., Murakami, Y., Shimabukuro, K., Wongratwanich, P., Verdonschot, R. G., Kakimoto, N., & Nagata, Y. (2021). Treatment outcomes of real-time intraoral sonography-guided implantation technique of ^{198}Au grain brachytherapy for T1 and T2 tongue cancer. Journal of Radiation Research, 62, 871–876. https://doi.org/10.1093/jrr/rrab059

Kostelnik, T. I., & Orvig, C. (2019). Radioactive Main Group and Rare Earth Metals for Imaging and Therapy. In Chemical Reviews, 119, 902–956. https://doi.org/10.1021/acs.chemrev.8b00294

Lawrence, E. O., & Livingston, M. S. (1932). The production of high-speed light ions without the use of high voltages. Physical Review, 40, 19. https://doi.org/10.1103/PhysRev.40.19

Levkovski, V. N. (1991). Middle Mass Nuclides (A=40-100) Activation Cross Sections by Medium Energy (E=10-50 MeV) Protons and Alpha-Particles. (Experiment and Systematics).

Mausner, L. F., Kolsky, K. L., Joshi, V., & Srivastava, S. C. (1998). Radionuclide development at BNL for nuclear medicine therapy. Applied Radiation and Isotopes, 49, 285–294. https://doi.org/10.1016/S0969-8043(97)00040-7

Meija, J., Coplen, T. B., Berglund, M., Brand, W. A., de Bièvre, P., Gröning, M., Holden, N. E., Irrgeher, J., Loss, R. D., Walczyk, T., & Prohaska, T. (2016). Atomic weights of the elements 2013 (IUPAC Technical Report). Pure and Applied Chemistry, 88, 265-291. https://doi.org/10.1515/pac-2015-0305

Michel, R., Brinkmann, G., & Stueck, R. (1983). Measurement and Hybrid Model Analysis of Integral Excitation Functions for α-Induced Reactions on Vanadium and Manganese. Nuclear Data for Science and Technology, 1, 599-602. https://doi.org/10.1007/978-94-009-7099-1_129

Murata, T., Aikawa, M., Saito, M., Ukon, N., Komori, Y., Haba, H., & Takács, S. (2019). Production cross sections of Mo, Nb and Zr radioisotopes from α-induced reaction on ^{nat}Zr. Applied Radiation and Isotopes, 144, 47–53. https://doi.org/10.1016/J.APRADISO.2018.11.012

Myers, W. G. (1979). Georg Charles de Hevesy: the father of nuclear medicine. Journal of Nuclear Medicine, 20, 590.

National Nuclear Data Center. (2021). Nuclear structure and decay data on-line library, Nudat 3.0 [WWW Document]. URL https://www.nndc.bnl.gov/nudat3

Neuzil, E. F., & Lindsay, R. H. (1963). Emission of ^{7}Be and competition processes at 30 to 42 MeV. Physical Review, 131, 1697-1701. https://doi.org/10.1103/PhysRev.131.1697

Otuka, N., & Takács, S. (2015). Definitions of radioisotope thick target yields. Radiochimica Acta, 103, 1-6. https://doi.org/10.1515/ract-2013-2234

Peng, X., He, F., & Long, X. (1999). Excitation functions for α-induced reactions on vanadium. Nuclear Instruments and Methods in Physics Research, Section B: Beam Interactions with Materials and Atoms, 152, 432-436. https://doi.org/10.1016/S0168-583X(99)00179-2

Pijarowska-Kruszyna, J., Pocięgiel, M., & Mikołajczak, R. (2022). Radionuclide generators. Nuclear Medicine and Molecular Imaging, 1, 66–78. https://doi.org/10.1016/B978-0-12-822960-6.00005-3

Qaim, S. M. (2004). Use of cyclotrons in medicine. Radiation Physics and Chemistry, 71, 917–926. https://doi.org/10.1016/J.RADPHYSCHEM.2004.04.124

Qaim, S. M. (2012). The present and future of medical radionuclide production. Radiochimica Acta, 100, 635–651. https://doi.org/10.1524/ract.2012.1966

Qaim, S. M., Scholten, B., & Neumaier, B. (2018). New developments in the production of theranostic pairs of radionuclides. In Journal of Radioanalytical and Nuclear Chemistry, 318, 1493–1509. https://doi.org/10.1007/s10967-018-6238-x

Rama, R. J., Mohan Rao, A. V., Mukherjee, S., Upadhyay, R., Singh, N. L., Agarwal, S., Chaturvedi, L., & Singh, P. P. (1987). Non-equilibrium effects in alpha-particle-induced reactions in light, medium and heavy nuclei up to 120 MeV. Journal of Physics G: Nuclear Physics, 13, 535-542. https://doi.org/10.1088/0305-4616/13/4/017

Ramogida, C. F., & Orvig, C. (2013). Tumour targeting with radiometals for diagnosis and therapy. Chemical Communications, 49, 4720-4739. https://doi.org/10.1039/c3cc41554f

Showaimy, H., Solieman, A. H. M., Hamid, A. S. A., Khalaf, A. M., & Saleh, Z. A. (2019). Measurements of activation cross sections for proton induced reactions on natural platinum targets leading to the formation of gold radioisotopes. Radiation Physics and Chemistry, 157, 97-101. https://doi.org/10.1016/j.radphyschem.2018.12.024

Singh, N. L., Agarwal, S., & Rao, J. R. (1993). Excitation function for α-particle-induced reactions in light-mass nuclei. Canadian Journal of Physics, 71, 115-121. https://doi.org/10.1139/p93-017

Singh, N. L., Mukherjee, S., Mohan Rao, A. V., Chaturvedi, L., & Singh, P. P. (1995). Effects of pre-equilibrium nucleon emission on excitation functions of various reactions in vanadium induced by alpha particles. Journal of Physics G: Nuclear and Particle Physics, 21, 399-410. https://doi.org/10.1088/0954-3899/21/3/014

Smith, S. V., McCutchan, E., Gürdal, G., Lister, C., Muench, L., Nino, M., Sonzogni, A., Herman, M., Nobre, G., Cullen, C., Chillery, T., Chowdury, P., & Harding, R. (2017). Production of platinum radioisotopes at Brookhaven Linac Isotope Producer (BLIP). EPJ Web of Conferences, 146, 09029. https://doi.org/10.1051/epjconf/201714609029

S.M. Qaim, F. Tárkányi, & R. Capote. (2012). Nuclear Data for the Production of Therapeutic Radionuclides (IAEA, Technical Reports Series-473). [WWW Document]. URL https://www.iaea.org/publications/8522/nuclear-data-for-the-production-of-therapeutic-radionuclides

Sonzogni, A. A., Romo, A. S. M. A., Frosch, W. R., & Nassiff, S. J. (1992). A code to determine the energy distribution, the incident energy and the flux of a beam of light ions into a stack of foils. Computer Physics Communications, 69, 429–438. https://doi.org/10.1016/0010-4655(92)90181-W

Sonzogni, A. A., Romo, A. S. M. A., Mosca, H. O., & Nassiff, S. J. (1993). Alpha and deuteron induced reactions on vanadium. Journal of Radioanalytical and Nuclear Chemistry Articles, 170, 143–156. https://doi.org/10.1007/BF02134585

Sonzogni, A., & Pritychenko, B. (2003). Q-value Calculator (QCalc). NNDC, Brookhaven National Laboratory [WWW Document]. URL https://www.nndc.bnl.gov/qcalc/

Srivastava, S. C. (2012). Paving the Way to Personalized Medicine: Production of Some Promising Theragnostic Radionuclides at Brookhaven National Laboratory. Seminars in Nuclear Medicine, 42, 151–163. https://doi.org/10.1053/J.SEMNUCLMED.2011.12.004

Starovoitova, V. N., Tchelidze, L., & Wells, D. P. (2014). Production of medical radioisotopes with linear accelerators. Applied Radiation and Isotopes, 85, 39–44. https://doi.org/10.1016/J.APRADISO.2013.11.122

Tárkányi, F., Ditrói, F., Takács, S., Csikai, J., Hermanne, A., Uddin, M. S., Hagiwara, M., Baba, M., Shubin, Y. N., & Dityuk, A. I. (2004b). Activation cross-sections of light ion induced nuclear reactions on platinum: Proton induced reactions. Nuclear Instruments and Methods in Physics Research, Section B: Beam Interactions with Materials and Atoms, 226, 473-489. https://doi.org/10.1016/j.nimb.2004.06.042

Tárkányi, F., Hermanne, A., Takács, S., Shubin, Y. N., & Dityuk, A. I. (2004a). Cross sections for production of the therapeutic radioisotopes ^{198}Au and ^{199}Au in proton and deuteron induced reactions on ^{198}Pt. Radiochimica Acta, 92, 223-228. https://doi.org/10.1524/ract.92.4.223.35588

Tárkányi, F. T., Ignatyuk, A. V., Hermanne, A., Capote, R., Carlson, B. v., Engle, J. W., Kellett, M. A., Kibédi, T., Kim, G. N., Kondev, F. G., Hussain, M., Lebeda, O., Luca, A., Nagai, Y., Naik,

H., Nichols, A. L., Nortier, F. M., Suryanarayana, S. v., Takács, S., & Verpelli, M. (2019). Recommended nuclear data for medical radioisotope production: diagnostic positron emitters. Journal of Radioanalytical and Nuclear Chemistry, 319, 533–666. https://doi.org/10.1007/s10967-018-6380-5

Tárkányi, F, Takács S, Gul K, Hermanne A, Mustafa M.G, Nortier M, Obložinský P, Qaim S.M, Scholten B, Shubin Y.N, & Yousiang Z. (2007). Charged particle cross-section database for medical radioisotope production (updated version). IAEA-TECDOC-1211 [WWW Document]. URL https://www-nds.iaea.org/medical/medical-old/monitor_reactions.html

Van Dort, M., Rehemtulla, A., & Ross, B. (2008). PET and SPECT Imaging of Tumor Biology: New Approaches Towards Oncology Drug Discovery and Development. Current Computer Aided-Drug Design, 4, 46 - 53. https://doi.org/10.2174/157340908783769265

Vlieks, A. E., Morgan, J. F., & Blatt, S. L. (1974). Total cross sections for some (α, n) and (α, p) reactions in medium-weight nuclei. Nuclear Physics, Section A, 224, 492-502. https://doi.org/10.1016/0375-9474(74)90551-X

Vonach, H., Haight, R. C., & Winkler, G. (1983). (α, n) and total α-reaction cross sections for ^{48}Ti and ^{51}V. Physical Review C, 28, 2278-2285. https://doi.org/10.1103/PhysRevC.28.2278

Watanabe, T., Fujimaki, M., Fukunishi, N., Imao, H., Kamigaito, O., Kase, M., Komiyama, M., Sakamoto, N., Suda, K., Wakasugi, M., & Yamada, K. (2014). Beam energy and longitudinal beam profile measurement system at the RIBF. IPAC 2014: Proceedings of the 5th International Particle Accelerator Conference, 3566-3568. doi:10.18429/JACoW-IPAC2014-THPME136

Werner, R. A., Bluemel, C., Allen-Auerbach, M. S., Higuchi, T., & Herrmann, K. (2015). ^{68}Gallium- and ^{90}Yttrium-/^{177}Lutetium: “theranostic twins” for diagnosis and treatment of NETs. Annals of Nuclear Medicine, 29, 1–7. https://doi.org/10.1007/s12149-014-0898-6

Ziegler, J. F., Ziegler, M. D., & Biersack, J. P. (2010). SRIM - The stopping and range of ions in matter (2010). Nuclear Instruments and Methods in Physics Research, Section B: Beam Interactions with Materials and Atoms, 268, 1818-1823. https://doi.org/10.1016/j.nimb.2010.02.091